

VIBRATION TESTING BY DESIGN:
EXCITATION AND SENSOR PLACEMENT
USING GENETIC ALGORITHMS

By

CINNAMON BUCKELS LARSON

A DISSERTATION PRESENTED TO THE GRADUATE SCHOOL
OF THE UNIVERSITY OF FLORIDA IN PARTIAL FULFILLMENT
OF THE REQUIREMENTS FOR THE DEGREE OF
DOCTOR OF PHILOSOPHY

UNIVERSITY OF FLORIDA

1996

To Jim and Audrey

ACKNOWLEDGEMENTS

I would like to sincerely thank my advisor, Dr. David Zimmerman, for all of the support, advice, and knowledge he has given to me. He has worked hard on my behalf, obtaining funding for my support and providing me with several research opportunities. He gave me the guidance to learn and the room to grow. I will forever be indebted to him.

I would like to thank my husband, Jim, his parents, and my daughter, Audrey. Without their love and support I never would have made it. I would like to thank my sisters, Beth, Kim, Cynthia, and Erin, my brother Laing, and my best friend Leslie for their never-ending encouragement and love. I am truly blessed.

I would like thank my dear friends Mohamed Kaouk and William Leath for their advice, support, and companionship through graduate school. I would also like to thank the entire staff and faculty of the Aerospace Engineering, Mechanics, and Engineering Science department. Specifically, I would like to acknowledge my committee, Dr. Norman Fitz-Coy, Dr. Daniel Drucker, Dr. Marc Hoit, Dr. Peter Ifju, and Dr. Bavani Sankar for their advice.

I would like to acknowledge Sandia National Laboratories for their financial support and for the research opportunities they have given me. Specifically, I would like to thank Ed Marek, Clay Fulcher, and Scott Klenke. I would also like to acknowledge General Motors for providing data for my studies.

I would like to thank the Florida/NASA Space Grant Consortium whose financial support made my graduate studies possible.

TABLE OF CONTENTS

	<u>page</u>
ACKNOWLEDGEMENTS	iii
LIST OF TABLES	vii
LIST OF FIGURES	viii
KEY TO ABBREVIATIONS	xi
ABSTRACT	xii
CHAPTERS	
1 INTRODUCTION	1
1.1 Finite Element Model Refinement	2
1.2 Modal Testing: Sensor and Actuator Placement	5
1.3 Current Study Objective	7
2 GENETIC ALGORITHMS: THEORY AND APPLICATION	9
3 FINITE ELEMENT MODEL REFINEMENT USING GENETIC ALGORITHMS	14
3.1 Introduction	14
3.2 Model Refinement Problem Formulation	14
3.3 Genetic Algorithm Application	15
3.4 Numerical Example: Six Bay Truss FEM	17
3.4.1 Model Refinement	18
3.4.2 Effect of Noise	20
3.5 Conclusions	22
4 MODAL TEST EXCITATION AND SENSOR PLACEMENT: CURRENT TECHNIQUES	25

4.1	Introduction	25
4.2	Effective Independence	25
4.3	Kinetic Energy	29
4.4	Eigenvector Product	31
4.5	Driving Point Residue	31
5	MODAL TEST EXCITATION AND SENSOR PLACEMENT: NEW TECHNIQUES	35
5.1	Introduction	35
5.2	Mode Indicator Function	35
5.2.1	Excitation Placement	36
5.2.2	Sensor Placement	39
5.3	Observability and Controllability	40
5.3.1	Excitation Placement	45
5.3.2	Sensor Placement	47
6	PRE-MODAL TEST PLANNING ALGORITHM APPLICATION: NASA EIGHT-BAY TRUSS	49
6.1	Introduction	49
6.2	NASA Eight-Bay Test Bed	49
6.2.1	Excitation Placement	50
6.2.2	Sensor Placement	54
6.2.3	Results: Random Sensor Location	57
6.3	Computational Efficiency	58
6.4	Conclusion	60
7	PRE-MODAL TEST PLANNING ALGORITHM APPLICATION: MICRO-PRECISION INTERFEROMETER TRUSS	61
7.1	Introduction	61
7.2	Micro-Precision Interferometer Test Bed	61
7.3	Excitation Placement	62
7.4	Sensor Placement	70
7.4.1	Unconstrained Sensor Placement	71

7.4.2 Triaxially Constrained Sensor Placement	76
7.4.3 Unconstrained vs. Triaxially-Constrained Sensor Sets	80
7.5 Effect of Model Error	80
7.5.1 Excitation Placement with Model Error	82
7.5.2 Sensor Placement with Model Error	83
7.6 Computational Cost	88
7.7 Conclusions	89
8 PRE-MODAL TEST PLANNING APPLICATION: CAR BODY	95
8.1 Introduction	95
8.2 Excitation Placement	95
8.3 Sensor Placement	102
9 CONCLUSIONS AND FUTURE WORK	105
REFERENCES	108
BIOGRAPHICAL SKETCH	112

LIST OF TABLES

<u>Table</u>	<u>page</u>
5.1 GMIF Design Variable Description	38
6.1 Eight-Bay Truss Frequencies and Mode Description	50
6.2 Percent Difference in FE and Identified Frequencies	57
6.3 Total Floating Point Calculations for Each Placement Technique	60
7.1 Reduced MPI FEM Frequencies Compared with MPI Modal Test Frequencies	64
7.2 Original, GMIF, and GCON Excitation Locations MIF Values	66
7.3 Difference Between Pre- and Post-Corrupted Model Frequencies and Mode Shapes	82
7.4 Number of Sensor or Triax Sets That Change When Model Error Is Added	87
7.5 Floating Point Calculations for MPI Sensor and Excitation Placement	89
8.1 Car Body Excitation Location and Orientation	96
8.2 Mode Indicator Function Values for Various Excitation Placements	97
8.3 Controllability Angles (in degrees) for Excitation Placements	101
8.4 Excitation Placement Techniques Floating Point Calculations	101
8.5 Triaxial Sensor Placement Techniques Floating Point Calculations	104

LIST OF FIGURES

<u>Figure</u>	<u>page</u>
1.1 Finite Element Modeling	2
1.2 Finite Element Model Refinement	3
1.3 Modal Testing	6
2.1 Genetic Algorithms as Robust Problem Solvers	9
2.2 Coding of a Four Design Variable Problem	11
2.3 Cross-Over Examples	12
2.4 Genetic Algorithm Flow Chart	13
3.1 Six Bay Truss with 25 DOFs	17
3.2 Generational Data, Measured Modes with No Noise	19
3.3 Generational Eigensolution Data, Measured Modes with No Noise	21
3.4 FRF after 0, 5, 10, and 20 Generations, Measured Modes with No Noise ...	21
3.5 Generational Data, Measured Modes with 15% Noise	23
3.6 Generational Eigensolution Data, Measured Modes with 15% Noise	23
3.7 FRF After 20 Generations, Measured Modes with 15% Noise	24
4.1 Typical Driving Point Residue (NASA 8-Bay Truss)	34
5.1 Typical MIF Plot	37
5.2 Excitation Selection by GMIF	38
5.3 State Space Variable Description	42
5.4 Controllability and Observability	44
6.1 NASA 8-Bay Truss	50
6.2 Eight-Bay Excitation Locations	51

6.3	Eight-Bay Excitation Locations Frequency Response of Time Domain Data	53
6.4	Eight-Bay Excitation Placement Cross-Orthogonality of Identified and FEM Modes 1 to 5	53
6.5	Eight-Bay Sensor Locations	55
6.6	Eight-Bay Sensor Placement Cross-Orthogonality of Identified and FEM Modes 1 to 5	56
6.7	Eight-Bay Cross-Orthogonalities of Five Techniques Compared to 300 Random Sensor Sets	59
7.1	MPI Structure	62
7.2	Excitation Placement on MPI Structure	63
7.3	Typical Frequency Response for MPI Structure	65
7.4	Comparison of Selected Excitation and Random Excitation MIF Values ...	68
7.5	Comparison of Selected Excitation and Random Excitation Controllability Angles	69
7.6	Cross-Orthogonality Between FE Modes and Identified Modes	70
7.7	Unconstrained MPI Sensor Sets	72
7.8	Cross-Orthogonality Between MPI FE and Identified Modes, 18 Unconstrained Sensors	74
7.9	Triaxially Constrained MPI Sensor Sets	77
7.10	Cross-Orthogonality Between MPI FE and Identified Modes, 6 Triaxially Constrained Sensors	78
7.11	Model Error Added to MPI FEM	81
7.12	True vs. Corrupted MPI Mode Shapes	81
7.13	GMIF Derived Excitation Locations	83
7.14	GCON Derived Excitation Locations	84
7.15	Model Error Effect on Unconstrained MPI Sensor Sets	85
7.16	Model Error Effect on Triaxially Constrained MPI Sensor Sets	86
7.17	Cross-Orthogonality Between MPI Identified Modes Using Corrupted Model and Uncorrupted FEM Modes (18 Unconstrained Sensors)	91

7.18	Cross-Orthogonality Between MPI Identified Modes Using Corrupted Model and Uncorrupted FEM Modes (6 Triaxially Constrained Sensors) . . .	93
8.1	Car Body Shaker Locations	96
8.2	MIF Values for Excitation Placements Compared to 500 Randomly Located 3-Point Excitations	99
8.3	Controllability Values for Excitation Placements Compared to 500 Randomly Located 3-Point Excitations	100
8.4	Triaxially Located Car Body Sensor Sets	102

KEY TO ABBREVIATIONS

AKE	average kinetic energy
ARS	average random sample
DOF	degree of freedom
DPR	driving-point residue
EI	effective independence
ERA	eigensystem realization algorithm
EVP	eigenvector product
FEM	finite element model
FRF	frequency response function
GA	genetic algorithm
GCON	genetic controllability algorithm
GMIF	genetic mode indicator function algorithm
GMRA	genetic model refinement algorithm
KE	kinetic energy
MIF	mode indicator function
MPI	micro-precision interferometer
OBS	observability

Abstract of Dissertation Presented to the Graduate School
of the University of Florida in Partial Fulfillment of the
Requirement for the Degree of Doctor of Philosophy

VIBRATION TESTING BY DESIGN:
EXCITATION AND SENSOR PLACEMENT
USING GENETIC ALGORITHMS

By

Cinnamon Buckels Larson

May 1996

Chairperson: Dr. David C. Zimmerman

Major Department: Aerospace Engineering, Mechanics and Engineering Science

This dissertation is an investigation of the use of genetic algorithms for the purposes of finite element model refinement and pre-modal test planning. The objective of a model refinement technique is to use information, about a structure, obtained during a vibration test to update the analytical model. The product of this process is an updated model of a structure which possesses dynamic properties closer to the dynamics obtained from the modal test of the structure. A genetic algorithm is used to vary finite element structural parameters to obtain an updated model with measured modal properties.

Although one purpose of a modal test is to use the information to update finite element models, the information obtained may be used for other purposes such as damage assessment, critical loads and frequency determination, and vibration control design. The type of information to be realized from a vibration test may well govern how and where the structure is excited and observed. The principal purpose of the current work is to explore the subject of pre-modal test planning for excitation and sensor placement. An overview of several existing sensor and excitation placement techniques is presented as a platform for the current study. The sensor placement techniques include effective independence, kinetic

energy, and eigenvector product and the excitation placement techniques include eigenvector product, kinetic energy, and driving-point residue. Two new sensor and two new excitation placement techniques are developed using normal mode indicator functions, and the concept of modal controllability and observability along with genetic algorithms. The new and existing techniques are compared using three finite element models: the NASA eight-bay truss, the Jet Propulsion Laboratory Micro-Precision Interferometer test bed, and a car body.

CHAPTER 1 INTRODUCTION

The area of structural engineering encompasses the design, manufacture, and test of a wide variety of systems. These basic steps are all used in the design of any structure, whether it is a household appliance, an automobile, a bridge, an aircraft, or a spacecraft. In the past, systems were over-engineered and over-built resulting in an increase in the time and material required to build them. Often times the steps in the engineering process were repeated several times until the designed system performed satisfactorily. With the advent of the computer, tools have been and are continuing to be developed which enable the structural engineer to improve on each step of the engineering process. These tools not only help to limit the time, material, and cost that it takes to complete the engineering steps but they also help to limit the repetition of these steps.

Structural computer modelling and vibration testing are two tools that have been developed with the aid of computers. Knowledge about material properties and structural dynamics may be used to create computer models of a system, which in turn may be used to predict dynamic performance and limitations. Once the system has been built, modal testing may be used to gain a greater insight into the dynamics of the structure and to update the computer model. An updated computer model may be used as a health monitoring tool for the structure after it goes into use.

1.1 Finite Element Model Refinement

One of the most common modelling techniques is finite element modelling (FEM) which can be used to represent the continuous medium of a structure as a connection of finite elements. This enables a system with distributed mass, damping, and stiffness properties to be represented as a lumped parameter system with discrete mass damping and stiffness properties (Figure 1.1). In other words, an infinite degree of freedom system is represented as a finite degree of freedom system.

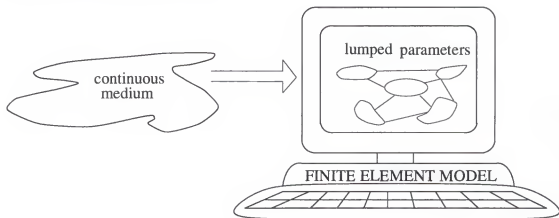


Figure 1.1 Finite Element Modeling

A wide variety of finite element modelling software is available to the designer. The basic steps involved in the modelling process are as follows:

1. Divide continuum into a finite number of elements.
2. Select node points where equilibrium conditions are enforced.
3. Determine element types and properties.
 - elemental type (rod, plate, etc.) and location
 - elemental displacement, stiffness, stress-strain, node-point loads
4. Assemble elemental matrices (mass, stiffness, and damping).
5. Develop equilibrium equations for node point location.

6. Create global mass damping and stiffness matrices from which frequencies and mode shapes are calculated.

The resulting FEM may be used to evaluate the efficacy of a design before it is built. Critical loads, resonant frequencies, and mode shapes may be predicted using the FEM and appropriate changes to the design based on these values may be made. Once the structure has been built, the FEM may be used to predict the performance of the structure under working conditions as well as serve as a damage assessment tool. However, while the original FEM is a predicted representation of a particular structure, the dynamic performance of the FEM very rarely matches the performance of the as-built structure. In order to correlate the dynamics of the structure to those of the FEM, the model must undergo a refinement process. The basic steps of FEM refinement are shown in Figure 1.2. The dynamic properties of the FEM are compared to the dynamic properties extracted from a vibration test of the structure. The resulting information is used to refine the model so that the modal properties of the FEM agree with modal properties from the vibration test.

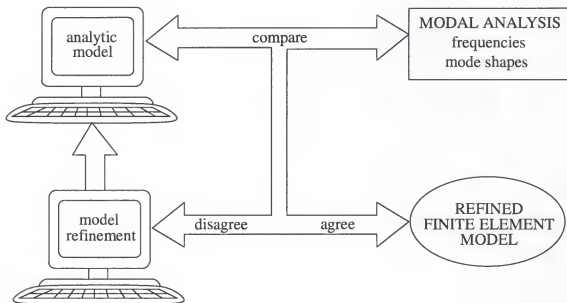


Figure 1.2 Finite Element Model Refinement

Some of the earliest work done in model refinement was proposed by Rodden (1967), who explored using modal test data to generate analytical mass and stiffness properties of the structure being tested. The early work of Rodden has broadened into the modern FEM refinement techniques. Algorithms used to address the FEM refinement can be broadly classified as falling into one of four different approaches: optimal-matrix updates, sensitivity methods, eigenstructure assignment techniques, and minimum-rank perturbation methods. Survey papers providing an overview of these techniques are provided in papers by Ibrahim and Saafan, 1987; Heylen and Sas, 1987; and Zimmerman and Kaouk, 1992.

In the optimal matrix update formulation, perturbation matrices for the mass, stiffness, and/or damping matrices are determined which minimize a given cost function subject to various constraints. Typical constraints may include satisfaction of the eigenproblem for all measured modes, definiteness of the updated property matrices and preservation of the original sparsity pattern of the property matrices. Baruch and Bar Itzhack (1978) worked on an optimal update of the global stiffness matrix with a cost function that minimized the Frobenius norm of the perturbation matrix. Their work was expanded to look at updating mass, damping, and stiffness matrices (Berman and Nagy, 1983; Fuh et al., 1984; Hanagud et al., 1984). Kabe (1985) and Kammer (1987) expanded on this work further by looking at matrix updating while preserving the sparsity pattern of the original FE global matrices.

Sensitivity methods for model refinement make use of sensitivity derivatives of modal parameters with respect to physical design variables (Martinez et al., 1991) or with respect to matrix element variables (Matzen, 1987). When varying physical parameters, the updated model is consistent within the original FE program framework. A variety of derivatives and optimization techniques have been used (Collins et al., 1974; Chen and Garba, 1980; Adelman and Haftka, 1986; Creamer and Hendricks, 1987; Flanigan, 1991). In the current work a physical parameter update technique using a genetic algorithm is developed.

Inman and Minas (1990) proposed designing pseudo-controllers to be applied to the FEM in an iterative fashion resulting in a match between measured and FE modal properties.

These controllers were then translated into matrix updates. These techniques, known as control-based eigenstructure assignment techniques, are based on work done in eigenstructure control (Andry et al., 1983). Zimmerman and Widengren (1990) proposed a non-iterative eigenstructure assignment formulation using an algebraic Riccati equation.

Finally, the development of a minimum rank update theory has been recently proposed as a computationally attractive approach for model refinement and damage detection (Zimmerman and Kaouk, 1992). The update to each property matrix is of minimum rank and is equal to the number of experimentally measured modes which the modified model is to match.

1.2 Modal Testing: Sensor and Actuator Placement

Regardless of the method used to perform FEM refinement, a modal test must be performed on a structure or its components in order to obtain the experimental information to correlate with the analytical information contained in the FEM. Finite element model refinement is only one use for modal data. Modal analysis is also a tool for damage assessment and force reconstruction. Several issues may govern the use of modal tests for these purposes. The final use of modal test data governs the pretest planning associated with modal testing. The placement of actuators for structural excitation purposes and the placement of sensors for structural response observations may well depend on whether the data will be used for modal parameter estimation, mode orthogonality for FEM correlation, identification of uncertain parameters in FEMs, structural health monitoring, or force reconstruction.

The science of modal testing is thoroughly discussed in D.J Ewins' book *Modal Testing: Theory and Practice*. The basic steps involved in a modal test are discussed here for completeness and are pictured in Figure 1.3. The structure being tested must be dynamically excited and the response of the structure to this input must be measured. The excitation may be accomplished using an impact hammer, a shaker, or a release from an initial structural

displacement. The response of the structure is generally measured using piezoelectric accelerometers, which are mounted on the structure in various locations. The force and response signals are sent to a processor or analyzer, after being filtered and amplified, from which a frequency response function (FRF) of the structure is obtained. The modal properties (mode shapes, damping ratios, and frequencies) may be obtained from the analysis of the FRF.

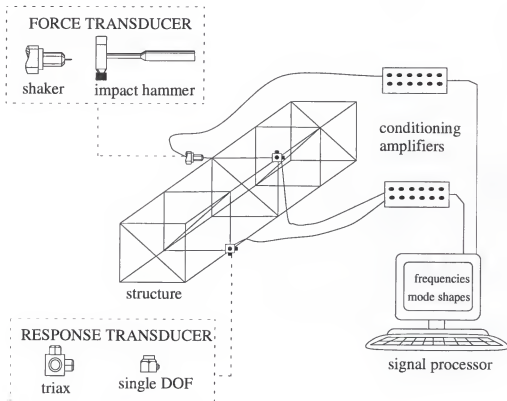


Figure 1.3 Modal Testing

Modal testing of a structure can be a costly venture in terms of time and money. Pre-modal test planning can be essential in saving cost by determining ahead of time the appropriate transducers and analyzers to use for the job at hand. Another aspect of pre-test planning, the one associated with the current study, is the optimal selection of the location of the force and response transducers. It is desired to obtain the most information at the least cost, which involves minimizing the number of transducers to be used. The selection of the

transducers will also depend on what the modal data will be used for (i.e., model refinement or damage detection).

A majority of the sensor placement research that has been done may be broadly classified into two areas, system identification and optimal control. Yu and Seinfeld (1973), Le Pourhiet and Le Letty (1978), Omatu et al. (1978), Sawaragi et al. (1978), and Qureshi et al. (1980) have all done work in the area of sensor placement for system identification. Shah and Udawadia (1978) and Udawadia and Garba (1985) have done work in sensor placement for structural parametric identification. Kammer (1991) approached the system identification sensor placement problem for the purpose of FEM validation. Goodson and Polis (1978) researched the selection of sensors for optimal structural control. Juang and Rodriguez (1979) looked at sensor placement for identification and control purposes.

Information about the FEM has been used by modal test designers to place sensors and actuators on a structure for the purpose of modal testing. Finite element DOFs which have high kinetic energy are good choices for sensor or actuator placement because more information may be extracted about and more energy may be input to the structure at these points (Kammer, 1991; Flanigan and Hunt, 1993; Lim, 1991). Jarvis (1991) proposes using FE mode shape products to find sensor and actuator locations for modal testing. Kientzy et al. (1989) used driving point residues or modal participation factors to determine modal test excitation locations. Mode indicator functions have been used by the modal test engineers to tune modes during a modal test (Hunt et al., 1984).

1.3 Current Study Objective

Proper modal test planning is needed in order to obtain the largest amount of information about a structure relative to the task of the data at the smallest cost. The refinement of finite element models is a task which benefits from modal test planning. The objective of the current studies is to explore the areas of finite element model refinement and

pre-modal test planning. Specifically, the use of the optimization technique, genetic algorithms (GAs), in these two areas will be examined.

The genetic algorithm is an optimization tool which has been developed in the past 20 years. An overview of the theory and applications of the GA is given in Chapter 2. A structural-parameter update model-refinement algorithm is developed using a genetic algorithm in Chapter 3 and is applied using a FEM of a two-dimensional truss structure.

The topics of pre-modal test planning actuator and sensor placement are examined in Chapters 4 and 5. In Chapter 4 several techniques which have been developed in existing literature are outlined. The excitation placement techniques of kinetic energy eigenvector product, and driving point residue and the sensor placement techniques of effective independence, kinetic energy, and eigenvector product are reviewed. In an effort to improve on the current sensor and actuator placement technologies, two new actuator and sensor placement techniques are developed in Chapter 5. The normal mode indicator function (MIF) of a FEM is used with a GA to optimally find excitation locations. In addition the MIF is used as a tool to locate sensors. The second sensor and actuator placement algorithms use a degree of controllability and observability calculated using the FEM information.

The effectiveness of the current sensor and actuator placement techniques and those developed in Chapter 5 are explored using several structural FEMs in Chapters 6,7, and 8. In Chapter 6 NASA's Eight-Bay truss, in Chapter 7 the micro-precision interferometer truss, and in Chapter 8 a FEM of a General Motors car body are used as examples to explore the effectiveness of all of the sensor and actuator placement algorithms for the purpose of pre-modal test planning. Concluding remarks and a discussion of future work in the areas outlined above are given in Chapter 9.

CHAPTER 2

GENETIC ALGORITHMS: THEORY AND APPLICATION

The motivation behind the development of GAs is that they are robust problem solvers for a wide class of problems, as depicted in Figure 2.1. However, it should be noted that they are not as efficient as nonlinear optimization techniques over the class of problems which are ideally suited for nonlinear optimization; namely continuous design variables with a continuous differentiable unimodal design space. Genetic Algorithms have the capability to solve continuous, discrete and a combination of continuous and discrete optimization problems.

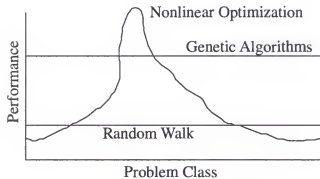


Figure 2.1 Genetic Algorithms as Robust Problem Solvers

Genetic algorithms are an optimization method which is based on Charles Darwin's survival of the fittest theories (Holland, 1975). The basic concept of the GA is that a population of designs is allowed to evolve over a period of time. The most fit members of that population are most likely to survive thus enabling their genetic code (or design information) to be passed down to future generations. More than just the information contained in the initial population may be passed down to future generations. As in nature as the evolutionary process progresses, mutations may occur in the offspring which may or may

not result in more fit population members. Ideally, this evolutionary process will result in a population of members more fit than the original initial population. Genetic Algorithms may therefore be described as a directed random search or as a compromise between determinism and chance.

Genetic algorithms are radically different from the more traditional design optimization techniques. Genetic algorithms work with a coding of the design variables, as opposed to working with the design variables directly. The search is conducted from a population of designs (i.e., from a large number of points in the design space), unlike the traditional algorithms which search from a single design point. The GA requires only objective function information, as opposed to gradient or other auxiliary information, which is usually required in other optimization techniques. The GA is based on probabilistic transition rules, as opposed to deterministic rules. There are five main operations in a basic GA: coding, evaluation, selection, crossover and mutation.

Coding is the process in which each design variable is coded as a q-bit binary number. Discrete variables would each be assigned a unique binary string. A continuous design variable B_i is approximated by 2^q discrete numbers between lower and upper bounds for the design variable,

$$B_i = B_{imin} + \frac{\text{binary\#}}{2^q - 1} (B_{imax} - B_{imin}) \quad (2.1)$$

where B_{imin} and B_{imax} are the lower and upper bounds on the i^{th} continuous design variable and binary# is an integer number between zero and $2^q - 1$. The continuous to discrete coding is like that of an analog to digital converter used in control systems. A population member is obtained by concatenating all design variables to obtain a single string of ones and zeros. Thus, a population member contains all information to completely specify the total design. For example, consider a design which has three continuous variables B_1 , B_2 and B_3 represented by 5-bit, 6-bit, and 4-bit numbers and a discrete design variable B_4 which can take on four different values. An example of a population of members containing this design

information is pictured in Figure 2.2. A population is defined to be a grouping of n_{pop} members, where n_{pop} is the number of members in the population.

population member	Design Variables			
	5 bit continuous B_1	6 bit continuous B_2	4 bit continuous B_3	2 bit discrete B_4
1	1 0 1 1 1	0 1 0 0 0 1	0 0 1 1	1 1
2	0 0 1 1 0	1 1 1 0 1 0	1 1 0 1	1 0
.
.
.
n_{pop}	1 1 0 1 0	0 1 1 0 0 0	0 0 1 1	0 1

Figure 2.2 Coding of a Four Design Variable Problem

Evaluation is the process of assigning a fitness measure to each member of the current population. The fitness measure is typically chosen to be related to the objective function which is to be minimized or maximized. No gradient or auxiliary information is used; only the value of the fitness function is needed. Therefore, GAs are less likely than traditional “hill climbing” algorithms to become “trapped” at a local minima or maxima. Additionally, because no gradient information is required, the design space is allowed to be discontinuous.

Selection is the operation of choosing members of the current generation to produce the prodigy of the next generation. Selection is biased toward the most fit members of the population. Therefore, designs which are better as viewed from the fitness function, and therefore the objective function, are more likely to be chosen as parents.

Crossover is the process in which design information is transferred to the prodigy from the parents. Crossover amounts to a swapping of various strings of ones and zeroes between the two parents to obtain two children. Two possible types of cross-over are illustrated in Figure 2.3.

	Point Cross-over	Pattern Cross-over
parent 1	1 0 1 0 0 0 1	1 0 1 0 0 0 1
parent 2	1 1 1 0 1 0 0	1 1 0 0 1 0 0
	<div style="text-align: center;"> swap point </div>	<div style="text-align: center;"> swap pattern x x - - x - x </div>
child 1	1 0 1 0 1 0 0	1 1 1 0 1 0 0
child 2	1 1 1 0 0 0 1	1 0 0 0 0 0 1

Figure 2.3 Cross-Over Examples

Mutation is a low probability random operation that may perturb the design represented by the prodigy. The mutation operator is used to retain design information over the entire domain of the design space during the evolutionary process.

Holland (1975) developed the concept of schema, which for a very simple GA implementation explains why GAs work. Schema are a similarity template defined by 0's, 1's and x's, where x's are the don't care symbol. Thus, for a design coded with a total of 8-bits, one schema would be 10xxxxxx. All designs which have a 1 in the most significant bit and a 0 in the 2nd most significant bit would be said to contain this schema. Holland's Schema Convergence Theorem states that under certain combinations of selection, crossover, and mutation, the expected number of schema H at generation k+1, $n(H, k+1)$, is given as

$$n(H, k + 1) \geq (1 - \epsilon) \frac{\text{fit}_H}{\text{fit}_{\text{avg}}} n(H, k) \quad (2.2)$$

where ϵ is a number much less than 1 and fit_H and fit_{avg} are the average fitness of all designs containing schema H and of the population as a whole, respectively. Thus, if those designs which contain schema H have on the whole a higher average fitness than the overall general population, the expected number of schema H in the next generation will be greater than or equal to the number of schema H in the current generation.

The proof is valid only for a specific combination of selection, crossover and mutation. It should be noted that a general proof for more complex GAs has not been developed. However, there exists a wide body of literature which demonstrates the power and capability of advanced GAs (Schaffer 1989, Grefenstette 1987). A flow chart summarizing the GA process is shown in Figure 2.4.

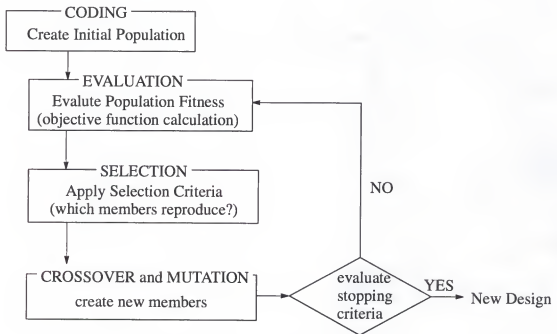


Figure 2.4 Genetic Algorithm Flow Chart

CHAPTER 3 FINITE ELEMENT MODEL REFINEMENT USING GENETIC ALGORITHMS

3.1 Introduction

As discussed in Chapter 1, an important tool in the design of engineering structures is the finite element model (FEM). Recall that FEM refinement techniques may be classified as optimal matrix updates, sensitivity updates, eigenstructure assignment updates, and minimum-rank perturbation updates. Sensitivity methods use sensitivity derivatives of modal parameters with respect to physical design variables or with respect to matrix element variables. These derivatives are used in order to determine what changes to make to the physical parameters or elemental matrices of the FEM in order to obtain a refined model with measured modal properties. A GA-driven model refinement technique is developed to update FE structural parameters to provide an updated model with the measured modal characteristics. This model refinement technique is illustrated using a numerical example.

3.2 Model Refinement Problem Formulation

For a given undamped structure it is assumed that an n -DOF FEM is developed and results in the second-order linear differential equation of motion,

$$\mathbf{M}\ddot{\mathbf{x}} + \mathbf{K}\mathbf{x} = \mathbf{0} \quad (3.2.1)$$

where \mathbf{M} and \mathbf{K} are the original analytic ($n \times n$) mass and stiffness matrices, and \mathbf{x} is the ($n \times 1$) position vector. The over-dots represent differentiation with respect to time. The eigenvalue problem associated with Eq. (3.2.1) can be written as

$$\lambda_r^2 \underline{M} \underline{\phi}_r + \underline{K} \underline{\phi}_r = \underline{0} \quad (3.2.2)$$

where λ_r is the r^{th} eigenvalue and $\underline{\phi}_r$ is the r^{th} mass orthogonal eigenvector of the original analytical system. It is assumed that the original analytic model of Eq. (3.2.1) does not satisfy the eigenvalues (λ_{mr}) and the mass orthogonal eigenvectors ($\underline{\phi}_{mr}$) of the experimentally measured system,

$$\lambda_{mr}^2 \underline{M}_m \underline{\phi}_{mr} + \underline{K}_m \underline{\phi}_{mr} = \underline{0} \quad (3.2.3)$$

where \underline{M}_m and \underline{K}_m are the experimentally derived mass and stiffness matrices of the structure. Therefore, a discrepancy between the original analytic and measured modal information will result in an eigenvalue problem of the form

$$\lambda_{mr}^2 [\underline{M} + \Delta \underline{M}(\underline{p})] \underline{\phi}_{mr} + [\underline{K} + \Delta \underline{K}(\underline{p})] \underline{\phi}_{mr} = \underline{0} \quad (3.2.4)$$

where $\Delta \underline{M}(\underline{p})$ and $\Delta \underline{K}(\underline{p})$ are perturbation matrices which are functions of the structural parameters vector \underline{p} . These perturbation matrices represent the mismatch between the original analytic mass and stiffness matrices and the experimentally derived mass and stiffness matrices. In order to develop an updated analytical model which is in agreement with measured modal data, a structural parameters vector \underline{p} must be found which satisfies Eq. (3.2.4) for all measured modes. In the following sections, a model refinement technique is developed which employs the use of a GA to find the structural parameters vector which will result in an updated FEM whose modal properties match the measured modal properties of the as-built structure.

3.3 Genetic Algorithm Application

As explained in Chapter 1, a FEM is a lumped parameter representation of a continuous structure. Information about the geometry and material of a structure are used to estimate its properties and to create the FEM. Mass, density, Young's modulus, cross-sectional area, and moment of inertia are some example of the properties which are used to develop a FEM.

Since these properties are estimated for the structure, they may be perturbed to give an updated FEM with the same modal properties as experimentally measured from the true structure. A Genetic Model Refinement Algorithm (GMRA) is developed which uses a GA to search for updated structural parameters which will result in an updated FEM with corresponding measured modal properties. An outline of the steps of GMRA, which follow those for a GA given in Chapter 2, follows.

Coding. The design variables used in GMRA are continuous design variables which represent the structural parameters to be changed. Limits may be set on the amount of perturbation allowed for each design variable or structural parameter. This enables the user to allow small perturbations to variables about which they are certain, such as cross-sectional area or moment of inertia and larger perturbations to variables about which they are less certain, such as density or Young's modulus.

Evaluation. The most fit members of a population are those which minimize a chosen objective function. An objective function has been formulated which states, the most fit structural parameters vector \mathbf{p} is one which results in an updated analytical model which gives the smallest value for the objective function

$$J_{\text{obj}} = \sum_{r=1}^n \frac{|\lambda_{ur} - \lambda_{mr}|}{\lambda_{mr}} w_r + \sum_{r=1}^n \|\underline{\phi}_{ur} - \underline{\phi}_{mr}\| h_r \quad (3.3.1)$$

where λ_{ur} and $\underline{\phi}_{ur}$ are the r^{th} eigenvalue and eigenvector of the updated analytical model. The first summation of Eq. (3.3.1) provides for the minimization between measured eigenvalues and updated analytic eigenvalues. As the updated eigenvalue approaches the measured eigenvalue the first summation approaches zero. The absolute value of the difference in each measured and updated eigenvalue is divided by the corresponding measured eigenvalue to insure that each frequency contributes equally to the objective function. The second summation of Eq. (3.3.1) is the 2-norm between the difference in measured and updated eigenvectors and provides for the minimization between measured and updated mode shapes. As the updated eigenvector approaches the measured eigenvector

the second summation approaches zero. The variables w_r and h_r are weights which can be changed in order to emphasize agreement between specific measured and updated eigenvalues/eigenvectors. By changing the weights, emphasis can be placed either on updated eigenvalue or updated eigenvector agreement with measured data.

3.4 Numerical Example: Six Bay Truss FEM

A finite element model of a six bay truss with 25-DOFs was developed to test GMRA. A picture of the truss is given in Figure 3.1.

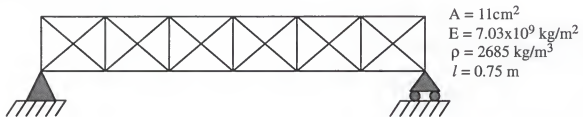


Figure 3.1 Six Bay Truss With 25 DOFs

In Figure 3.1, A is the cross sectional area, E is the modulus of elasticity, ρ is the density of all of the members, and l is the length of each bay. It is assumed that the analytic model is incorrect and needs to be changed in order to facilitate agreement in analytic and measured modal properties. To obtain experimental modal information, the FEM of the six bay truss is altered and the “experimental” modal information is calculated. It is assumed that the dimension of the measured eigenvector is the same as that of the analytic eigenvector. This can be accomplished using an eigenvector expansion algorithm (Berman and Nagy, 1971; Smith and Beatie, 1990; Zimmerman and Smith, 1992). An alternate formulation would be to let the vector norm calculation of Eq. (3.3.1) take place over only those components of the eigenvector that are measured, therefore, eliminating any error that may be introduced by expanding the measured eigenvectors.

3.4.1 Model Refinement

As a first example, it is assumed that all of the structural parameters are known to be correct except for E , the modulus of elasticity. In addition, the properties of all of the diagonal members, all of the horizontal members, and all of the vertical members are linked. GMRA is used to find the updated structural parameters vector, \underline{p}_u , which minimizes Eq. (3.3.1),

$$\underline{p}_u = \{E_d \ E_h \ E_v\} \quad (3.4.1)$$

The components of \underline{p}_u (E_d , E_h , and E_v) are the moduli of elasticity of the diagonal, horizontal, and vertical truss members. The original analytic model has the same modulus of elasticity for all members, which will be referred to as E_{nom} . The resulting analytical parameters vector is

$$\underline{p}_A = \{E_{nom} \ E_{nom} \ E_{nom}\} \quad (3.4.2)$$

The value for E_{nom} is $7.03 \times 10^9 \text{ kg/m}^2$. The structural parameters vector which is used to generate the experimentally measured model is

$$\underline{p}_m = \{0.95E_{nom} \ 0.90E_{nom} \ 0.92E_{nom}\} \quad (3.4.3)$$

The genetic algorithm is instructed to search for three design variables (components of the structural parameters vector) which are in the range of $0.7E_{nom}$ to $1.3E_{nom}$. An initial population representing the horizontal, vertical, and diagonal moduli of elasticity is randomly generated within the limits of $0.7E_{nom}$ to $1.3E_{nom}$. A member is added to this initial population which represents the original analytic model parameters vector. Since the original population is randomly generated, there is a good possibility that one of those initial population members will be more fit than the member representing the original analytic model. Therefore, the improvement in the updated eigensolution would in part be due to a random search. Even though this random chance is a benefit of genetics, in order to show the true improvement to the original analytic model by the genetic algorithm, an initial

population is chosen with all members less fit than the member representing the original analytic model. In order to facilitate frequency matching, the weights of Eq. (3.3.1) are set to emphasize minimization of the eigenvalue portion of the cost function. Five measured modes are supplied and GMRA is instructed to run for twenty generations (Figure 3.2).

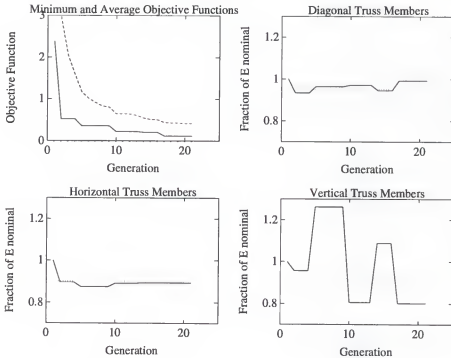


Figure 3.2 Generational Data, Measured Modes with No Noise

The top left graph of Figure 3.2 shows the average fitness (dashed line) and maximum fitness (solid line) of the current population at each generation. As the generations increase the average and maximum fitness improves, which corresponds to a decrease in the value of the objective function. After the first generation there is substantial improvement in the updated objective function over the original analytic objective function value. Since the members of the population which are randomly generated are all less fit than the original analytical model member, the decrease in objective function over the first generation is due to the children of the initial population. Since it is the goal to minimize the objective function, this is a desirable trend. Also as the generation increases, the average fitness approaches the maximum fitness. This is due to the fact that as generations evolve, the

overall population tends toward the most fit member. After a certain number of generations, the diversity in the population members decreases.

The other three graphs of Figure 3.2 show how the actual design variables (moduli of elasticity) are varying over the generations. The straight lines on these graphs correspond to the “experimental” diagonal, horizontal, and vertical moduli of elasticity which were used to generate the measured modes. It is seen that within the first few generations, the parameters have quickly converged near their “experimental” values. In later generations it is seen that E_v , the vertical member’s elastic modulus, varies widely. Physically, this is due to the fact the lower modes are fairly insensitive to the stiffness of the vertical members.

The generational trends of the eigensolution of the updated model are shown in Figure 3.3. The top left graph is the norm of the difference in the measured and updated eigenvectors. It can be seen that over some of the generations the value of this norm increases instead of decreasing. This is due to the fact that the eigenvalue portion of the cost function is weighted more heavily in order to insure modal frequency agreement. It can be seen that an increase in the norm in Figure 3.3 corresponds to the overall updated eigenvalues moving closer to the measured eigenvalues resulting in a decrease in the value of the objective function. A comparison of the first three frequencies of the updated model with respect to the measured frequencies over 20 generations is shown in the other three graphs of Figure 3.3.

The FRFs of the pre-genetics model and the FRFs of the post-genetic models after 0, 5, 10, and 20 generations are pictured in Figure 3.4. An immediate improvement in the FRF of the system can be seen after five generations.

3.4.2 Effect of Noise

The example presented would be expected to behave differently when there is noise present in the measured modal information. To simulate noise in the measured data, 5% and 15% random noise were added to the measured eigenvectors. It is assumed that the modal frequencies are measured accurately. As in the case with no noise, an initial population is

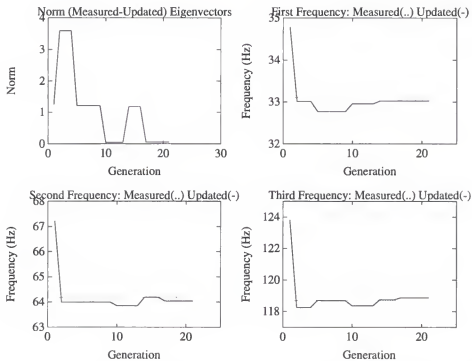


Figure 3.3 Generational Eigensolution Data, Measured Modes with No Noise

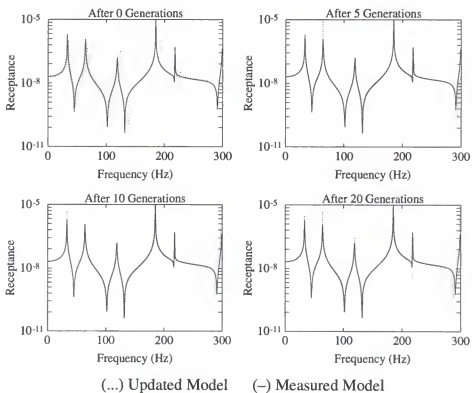


Figure 3.4 FRF After 0, 5, 10, and 20 Generations, Measured Modes with No Noise

generated with one member which represents the original analytic model and with other members randomly generated which have cost function values greater than that for the original analytic model member. This is to show how the cost function is minimized due to genetics and not just due to a random selection of a more fit design. GMRA was run using 5% and 15% noise with 5 measured modes. The generational results for 15% noise are pictured in Figures 3.5 and 3.6, and the FRF is pictured in Figure 3.7. Graphically a similar trend was observed for 5% noise.

An immediate improvement in the cost function can be seen after 5 generations, as shown in the top left graph of Figure 3.5. The generational updated eigensolution data of Figure 3.6 shows a similar trend to that of the example with no noise. The norm of the difference in measured eigenvectors with 15% noise and the updated eigenvectors is given in the top left graph of Figure 3.6. The straight dotted line in this figure corresponds to the norm of the difference in measured eigenvectors with and without noise.

The FRF pictured in Figure 3.7 shows how the model which was updated using noisy data compares with measured model without noise and with the original analytic model. Because the cost function was weighted to be more heavily affected by the frequencies, the effect that noisy modes may have had on the update was minimized.

3.5 Conclusions

One of the benefits of using a GA to search for an updated parameters vector is that the search is conducted from several points in the design space whereas conventional gradient sensitivity methods conduct the search from a single point. This helps enable GMRA to avoid getting stuck in a local minimum in addition to completing the search faster. Based on the evaluation of the data of this example, GMRA was successful in identifying an updated parameters vector which resulted in an updated FEM with measured modal properties. One, draw back to GMRA is that it requires an eigensolution of the FEM in order to calculate the objective function of Eq. (3.3.1). For large FEMs this objective function evaluation is a

computationally expensive calculation, and would need to be redesigned to make GMRA a feasible model refinement tool.

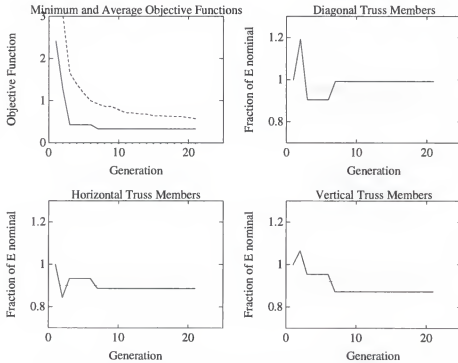


Figure 3.5 Generational Data, Measured Modes with 15% Noise

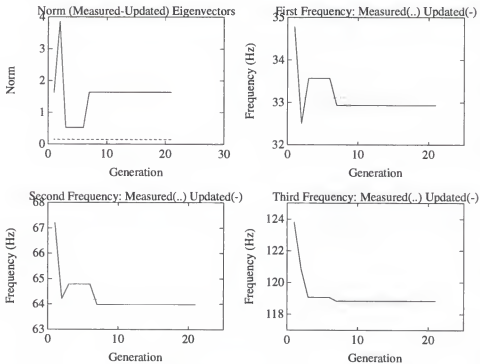


Figure 3.6 Generational Eigensolution Data, Measured Modes with 15% Noise

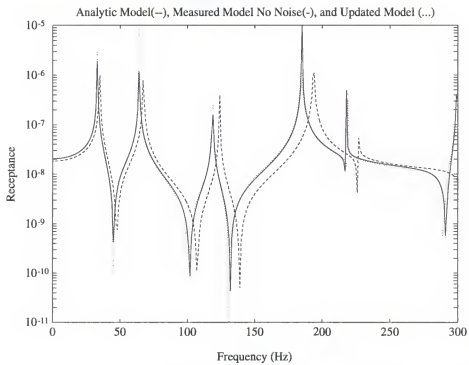


Figure 3.7 FRF After 20 Generations, Measured Modes with 15% Noise

CHAPTER 4

MODAL TEST EXCITATION AND SENSOR PLACEMENT: CURRENT TECHNIQUES

4.1 Introduction

In the current literature various techniques for excitation and sensor selection for modal testing exist. These techniques vary in computational complexity, cost, and accuracy. Several of these techniques were explored in the current study as a basis for comparison for the excitation and sensor placement techniques developed in the next chapter. An overview of the excitation placement techniques of kinetic energy, driving point residues, and eigenvector products and of the sensor placement techniques of effective independence, kinetic energy, and eigenvector product is given in the following sections.

4.2 Effective Independence

Effective independence (EI) is a technique developed to place sensors for the purpose of obtaining structural information for FEM verification for large space structures (Kammer, 1991). It follows from the work done by Shah and Udawadia (1978) and Udawadia and Garba (1985). The sensor locations are chosen such that the trace and determinant of the Fisher information matrix (corresponding to the target modal partitions) are maximized and the condition number minimized. By maximizing the determinant of the Fisher information matrix, the covariance matrix of the estimate error would be minimized, thus giving the best estimate of the structural response. A reduced sensor set is obtained in an iterative fashion from an initial candidate set by removing sensors from those DOFs (i.e., removing rows from the Fisher information matrix) which contribute least to the linear independence of the target modes.

In order to perform test analysis mode shape correlation using a cross-orthogonality criterion, the measured modes obtained during the modal test must be linearly independent. A summary of the derivation given in Kammer's paper (1991) follows. The output of the sensors can be expressed as the product between the FEM target mode matrix partitioned to a candidate set of sensors, Φ_s , and the modal coordinates q

$$u_s = \Phi_s q + \Psi_o^2 = H + \Psi_o^2 \quad (4.2.1)$$

with Gaussian white noise Ψ_o^2 added. It is assumed that the FEM mode shapes are linearly independent. The sensors are sampled and an estimate of the state of the system is calculated as

$$\hat{q} = [\Phi_s^T \Phi_s]^{-1} \Phi_s^T u_s \quad (4.2.2)$$

In order to obtain the best estimate of the state of the structure, the covariance matrix of the estimate error must be a minimum. The covariance matrix is given by

$$P = E[(q - \hat{q})(q - \hat{q})^T] = \left[\left(\frac{\delta H}{\delta q} \right)^T [\Psi_o^2]^{-1} \left(\frac{\delta H}{\delta q} \right) \right]^{-1} \quad (4.2.3)$$

Assuming that the sensors measure displacement (acceleration may also be considered), the covariance matrix may be rewritten as

$$P = \left[\Phi_s^T (\Psi_o^2)^{-1} \Phi_s \right]^{-1} = Q^{-1} \quad (4.2.4)$$

where Q is the Fisher information matrix and can be rewritten as

$$Q = \frac{1}{\Psi_o^2} \Phi_s^T \Phi_s = \frac{1}{\Psi_o^2} A_o \quad (4.2.5)$$

A_o will now be referred to as the Fisher information matrix. In order to minimize the covariance error P , Q must be maximized; therefore A_o must be maximized. Kammer (1991) states that the determinant of the Fisher information matrix for the best linear estimate is a maximum for all linear unbiased estimators. Therefore, one wishes to maximize the

determinant of the Fisher information matrix. From Eq. (4.2.5), the Fisher information matrix is calculated to be the product of the transpose of the target mode matrix times the target mode matrix,

$$A_o = \Phi_s^T \Phi_s \quad (4.2.6)$$

The first step is to calculate the eigenvalues λ_A and eigenvectors Ψ_A of the Fisher information matrix. Since it is assumed that the original FEM mode shapes are linearly independent, A_o will be positive definite, the eigenvalues will be real and positive and the eigenvectors will be orthonormal. The next step is to form the matrix product,

$$G = [\Phi_s \Psi_A] \otimes [\Phi_s \Psi_A] \quad (4.2.7)$$

where \otimes is an element by element multiplication. The columns of G sum up to be the eigenvalues of A_o . Next the G matrix is scaled by the inverse of the eigenvalues of A_o ,

$$F_E = G \begin{bmatrix} \backslash & & \\ & \lambda_A^{-1} & \\ & & \backslash \end{bmatrix} \quad (4.2.8)$$

The effective independence vector is then calculated by summing the rows of the F_E matrix,

$$E_D = \left\{ \begin{array}{c} \sum_{j=1}^n F_{E1j} \\ \sum_{j=1}^n F_{E2j} \\ \vdots \\ \sum_{j=1}^n F_{E(nDOF)j} \end{array} \right\} \quad (4.2.9)$$

where n is the number of target modes. The i^{th} term in the E_D vector is hypothesized to be the contribution of the i^{th} sensor to the linear independence of the FEM modes. A value of 1.0 in the E_D vector corresponds to a DOF that is essential to the linear independence of the target modes (i.e., that DOF must be retained as a measurement location). The DOF which

contributes least to the linear independence (i.e., lowest E_D value) is removed from the FEM target mode matrix. The Fisher information matrix A_o , the G and F_E matrices, and effective independence vector E_D are recalculated and the next sensor location is deleted from the target set. This iterative process is performed until the desired number of sensors remains. The minimum number of sensors required for identification corresponds to the number of target modes supplied.

The previously described technique chooses single DOFs to place sensors. Often times a modal tester uses triaxial sensors instead of single DOF sensors. Assume the FEM being used to place sensors has 3 DOF per node. The EI algorithm is modified to choose 3 DOFs at a time (corresponding to a node point) which contributed least to the linear independence of the target modes were eliminated over each iteration. The EI value for each node is calculated as a sum of the EI of each DOF of that node. The E_D values for the 3 DOFs at each node are summed as,

$$E_{D_{\text{triax}}} = \begin{bmatrix} E_D(1) + E_D(2) + E_D(3) \\ E_D(4) + E_D(5) + E_D(6) \\ \vdots \\ E_D(s-2) + E_D(s-1) + E_D(s) \end{bmatrix} \quad (4.2.10)$$

The 3 DOFs which contributes least to the linear independence (i.e., lowest $E_{D_{\text{triax}}}$ value) are removed from the FEM target mode matrix. However, if 1 of the DOFs for a particular node had an EI value of 1.0, meaning that that DOF was essential to the linear independence of the target modes, that node point would be retained, regardless of the ranking of its node point EI sum rating compared to the other node points. The Fisher information matrix A_o , the G and F_E matrices, and effective independence vector $E_{D_{\text{triax}}}$ are recalculated and the next triax sensor location is deleted from the target set. This iterative process is performed until the desired number of sensors remains.

It is suggested that to increase computational efficiency for large FEM, the original FEM should be reduced down to a candidate set of measurement locations larger than the number of sensors to be placed before performing the effective independence calculations.

One suggested technique for this reduction is modal kinetic energy, which is discussed in the next section.

4.3 Kinetic Energy

The use of kinetic energy for optimal sensor placement as well as target mode identification has been discussed in several papers (Salama et al., 1987; Kammer, 1991). The modal kinetic energy is calculated using the FEM mass matrix and target modes. The kinetic energy of the i^{th} DOF of the j^{th} mode is given as

$$KE_{ij} = \Phi_{ij} \sum_{k=1}^{n\text{DOF}} M_{ik} \Phi_{kj} \quad (4.3.1)$$

where Φ_{ij} is the ij^{th} entry of the FEM modal matrix Φ , M_{ik} is the ik^{th} entry of the FEM mass matrix M , and $n\text{DOF}$ is the total number of DOFs of the mass and modal matrices. The kinetic energy matrix, KE , can be expressed as the matrix product

$$KE = \Phi \otimes M \Phi = \begin{bmatrix} - KE_{\text{DOF1}} & - \\ - KE_{\text{DOF2}} & - \\ \vdots & \vdots \\ - KE_{\text{DOFn}} & - \end{bmatrix} \quad (4.3.2)$$

where \otimes denotes an element by element multiplication of the matrix Φ and the matrix resulting from the product of M and Φ . The rows of the KE matrix correspond to the DOFs of the model and the columns correspond to the modes of the FEM. Locations for actuation or sensing are chosen as those DOFs with a maximum value of kinetic energy for a given mode. For example, assume the Φ contains FEM modes 1 through 10 for a given structure and one wishes to sense or excite the third mode. The DOF (row) with a maximum kinetic energy value for the third mode or column of the KE matrix would be selected. It is assumed that by placing the sensors at points of maximum kinetic energy, the sensors will have the maximum observability of the structural parameters of interest.

If the modal test designer wishes to place triaxially constrained sensors, then a KE matrix may be calculated by summing the rows of Eq. (4.3.2) corresponding to DOFs for

each node. Then the node points with maximum KE over the modes of interest may be chosen as locations for actuators or sensors.

$$KE_{\text{triax}} = \begin{bmatrix} KE_{\text{DOF1}} + KE_{\text{DOF2}} + KE_{\text{DOF3}} \\ KE_{\text{DOF1}} + KE_{\text{DOF2}} + KE_{\text{DOF3}} \\ \vdots \\ KE_{\text{DOFn-2}} + KE_{\text{DOFn-1}} + KE_{\text{DOFn}} \end{bmatrix} \quad (4.3.3)$$

The kinetic energy objective function precludes placing any sensors or actuators at nodal points since there is no motion and zero kinetic energy at these points (i.e., the Φ entry would be zero resulting in a zero product). This could be a limiting factor in the pretest planning. To combat this problem, sensors can also be placed using maximum average kinetic energy (AKE) technique. A sensor is placed at a DOF with a maximum average kinetic energy over a range of modes of interest. In using an average kinetic energy, a DOF is not necessarily excluded if it is a node point of a particular mode. The average kinetic energy vector is calculated as

$$AKE = \left\{ \begin{array}{c} \sum_{k=1}^N KE_{1k} \\ \sum_{k=1}^N KE_{2k} \\ \vdots \\ \sum_{k=1}^N KE_{(\text{ndof})k} \end{array} \right\} / N \quad (4.3.4)$$

where N is the number of modes in the mode shape matrix Φ (i.e., the number of columns of the KE matrix). The sensor or actuator locations are found by finding the DOFs of the maximum average kinetic energies. Triaxially constrained sensors may be placed by taking the sum of the average kinetic energy for the DOFs for each node and choosing the nodes with maximum average kinetic energy.

In addition, it should be noted that the mass weighting inherent to the kinetic energy and average kinetic energy approaches causes the sensor or excitation placement to become dependent on the finite element discretization of the structure. There is an inherent bias

against the placement of sensors in the areas of the structure in which a fine mesh size (and thus small mass) is used.

4.4 Eigenvector Product

This technique uses modal products from the reduced FEM eigenvectors to identify possible locations for sensors or excitation. By choosing a frequency range of interest and the corresponding FEM eigenvectors (or modes) in that range, the eigenvector product is calculated as

$$\underline{EVP} = \left\{ \begin{array}{c} | \\ \phi_1 \\ | \end{array} \otimes \begin{array}{c} | \\ \phi_2 \\ | \end{array} \otimes \dots \otimes \begin{array}{c} | \\ \phi_N \\ | \end{array} \right\} \quad (4.4.1)$$

where \otimes represents an element by element multiplication of the mode shape vectors ϕ . The i^{th} entry of the EVP is given as

$$EVP_i = \phi_{i1}\phi_{i2}\phi_{i3} \dots \phi_{iN} \quad (4.4.2)$$

This product is calculated for all candidate DOF sensor or actuator locations. A maximum value of this product corresponds to a candidate location of reference or excitation (Jarvis, 1991). This technique also precludes the placement of sensors at nodal points which result in zero eigenvector products. If this presents a problem for a given test case, the eigenvector product can be replaced equivalently by an absolute value eigenvector sum, over the FE target modes of interest.

The eigenvector product may be used to place triaxially constrained sensors by summing up the entries of Eq. (4.4.2) which correspond to a particular node point. The node points with the maximum eigenvector product sum are then chosen as points of reference.

4.5 Driving Point Residue

A FEM can be used to identify the best locations and directions for exciting a structure by an evaluation of driving point residues (DPRs) or modal participation factors (Kientzy et

al, 1989). A DPR is a measure of how much a particular mode is excited at a particular DOF. The point and direction of excitation are chosen where the DPRs are maximized (to excite a given mode) or minimized (to avoid exciting a given mode). An equation of motion in Laplace domain for a structure may be written as

$$[Ms^2 + Cs + K]X(s) = F(s) \quad \text{or} \quad B(s)X(s) = F(s) \quad (4.5.1)$$

where M , C , and K are the $(n \times n)$ mass, damping and stiffness matrices, s is the complex Laplace variable ($s = \sigma + i\omega$), and $F(s)$ is the transformed excitation forces. Equation (4.5.1) may be solved for the transformed displacement responses, $X(s)$,

$$X(s) = H(s)F(s) \quad \text{where} \quad H(s) = B(s)^{-1} \quad (4.5.2)$$

and $H(s)$ is referred to as the transfer matrix. The system transfer matrix for a structure with damping can be expressed in the form

$$H(s) = \sum_{k=1}^N \frac{[R_k]}{s - \lambda_k} + \frac{[R_k^*]}{s - \lambda_k^*} \quad (4.5.3)$$

where R_k and R_k^* are the modal residues and λ_k and λ_k^* are the complex conjugate pairs of eigenvalues of the transfer matrix. The residues can be written in terms of the mode shapes ϕ_k as

$$H(s) = \sum_{k=1}^N \frac{A_k [\phi_k] [\phi_k]^T}{s - \lambda_k} + \frac{A_k^* [\phi_k^*] [\phi_k^*]^T}{s - \lambda_k^*} \quad (4.5.4)$$

where A_k is the mode shape scaling constant. For a structure which is lightly damped, the following two inequalities are true:

$$\sigma_k \ll \omega_k \quad \text{and} \quad \text{Imaginary}[\phi_k] \ll \text{Real}[\phi_k] \quad \text{for } k = 1 \text{ to } N \quad (4.5.5)$$

When these conditions are imposed, the mode shape scaling constants can be written in the form

$$A_k = \frac{1}{m_k \omega_k} \quad \text{for } k = 1 \text{ to } N \quad (4.5.6)$$

and the residues become

$$R_k(a, b) = \frac{[\phi_k(a)\phi_k(b)]}{(m_k\omega_k)} \quad \text{for } k=1 \text{ to } N \quad (4.5.7)$$

where $R_k(a, b)$ is the residue between DOF a and DOF b, $\phi_k(a)$ is the k^{th} mode shape component at DOF a, $\phi_k(b)$ is the k^{th} mode shape component at DOF b. If the mode shapes are scaled such that they are mass orthonormal, (i.e., $\Phi^T M \Phi = I$, where Φ is the matrix whose columns are the mode shapes ϕ_k (for $k=1$ to N), M is the FEM mass matrix, and I is the identity matrix) then the residues (in terms of the displacements) may be written as

$$R_k(a, a) = \frac{\phi_k(a)^2}{\omega_k} \quad \text{for } k=1 \text{ to } N \quad (4.5.8)$$

or equivalently in terms of acceleration

$$R_k(a, a) = \phi_k(a)^2 \omega_k \quad \text{for } k=1 \text{ to } N \quad (4.5.9)$$

The easiest way to evaluate several residues at once is to display them graphically. The DPRs that were calculated for the NASA 8-bay truss are shown in Figure 4.1. The DPRs are graphed in order of weighted average residue in order to discriminate against zero DPRs. The weighted average residue is calculated as

$$\text{waDPR} = \text{average DPR} \times \text{minimum DPR} \quad (4.5.10)$$

Each vertical line on the graph represents the range of DPRs from maximum to minimum over all the modes of interest for a single candidate DOF. The highest weighted average which is the best driving point is displayed first. The residues in the top graph are the square root of the sum of the squares of the residues in the x, y, and z direction plotted on a log scale. The bottom graphs are the residues for the x, y, and z direction plotted on unit normalized linear scales. The top graph is used to choose the node at which to place the excitation device. The bottom graphs are used to find the x, y, or z direction of the excitation.

In order to insure that an excitation location will give uniform participation of as many target modes as possible, it is desired to find a high average residue for a given DOF as well as

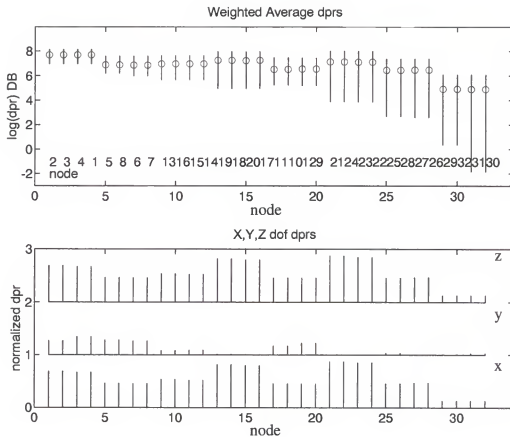


Figure 4.1 Typical Driving Point Residue (NASA 8-Bay Truss)

a small residue range over all the modes of interest. For this example the highest weighted average DPRs are at nodes 2, 3, 4, and 1 as seen in the top portion of Figure 4.1. The bottom portion of this figure shows that the optimal directions for excitation at these node points would be in the x and/or z direction, because the larger residues are in these directions.

CHAPTER 5 MODAL TEST EXCITATION AND SENSOR PLACEMENT: NEW TECHNIQUES

5.1 Introduction

In an effort to improve on the existing sensor and excitation placement techniques, two new sensor placement techniques and two new excitation techniques are developed in the current work. The first excitation and sensor placement techniques are based on the FEM normal Mode Indicator Function (MIF) calculation. The second excitation and sensor placement techniques are based on the observability and controllability calculations of the modes of the FEM. The effectiveness of these techniques, along with the techniques discussed in Chapter 4, will be explored in subsequent chapters using several different structural test-beds.

5.2 Mode Indicator Function

The mode indicator function (MIF) was first developed to detect the presence of real normal modes in sine dwell modal testing (Hunt et al, 1994 and Williams et al, 1985). This function also serves as a useful metric for pre-test analysis. While it is somewhat useful for assessing the efficacy of sensor layout, its true utility lies in assessing the effectiveness of a particular input in exciting the system modes.

The first step in calculating the MIF is the calculation of an acceleration frequency response function using the FEM mode shapes and frequencies,

$$H_{ik}(\omega) = \sum_{r=1}^m \frac{-\omega^2 \phi_i^r \phi_k^r}{ms_r(\omega_r^2 - \omega^2 + j2S_r\omega_r\omega)} \quad (5.2.1)$$

where m – number of modes in frequency range of interest

ϕ^r – r^{th} mode

ϕ_k^r – force input point k of the r^{th} mode

ϕ_i^r – response point i of the r^{th} mode

ω – discrete frequency at which to calculate H_{ik}

ω_r – frequency of the r^{th} mode

S_r – viscous damping ratio of r^{th} mode

m_{s_r} – modal mass of the r^{th} mode

Next, the normal MIF is calculated using H_{ik} as

$$\text{MIF}(\omega) = \frac{\sum_{i=1}^L (|\text{Real}(H_{ik}(\omega))| \times |H_{ik}(\omega)|)}{\sum_{i=1}^L (|H_{ik}(\omega)|^2)} \quad (5.2.2)$$

where L is the total number of response points. The MIF is nearly 1.0 except near a normal mode, at which point it drops off considerably since the frequency response becomes mostly imaginary at that point (i.e., $\text{Real}(H_{ik}(\omega))$ is very small). A plot of a typical MIF is given in Figure 5.1.

5.2.1 Excitation Placement

In pre-test planning, an excitation is desired which exhibits a sharp drop in the MIF at each mode of interest, indicating that the mode is well excited. The Genetic Mode Indicator Function (GMIF) excitation selection algorithm uses a genetic algorithm (Holland, 1975) to find excitation locations and their orientations on a structure to optimally excite a given mode or range of modes. The success of the excitation is based on the MIFs of the chosen excitation locations. If more than one excitation is sought then a MIF must be calculated for each. A single excitation need not exhibit a sharp MIF drop for all modes as long as the union of the MIFs for all of the excitation sources exhibits a large drop for each target mode. Two algorithms have been developed. The first is an unconstrained version which searches for

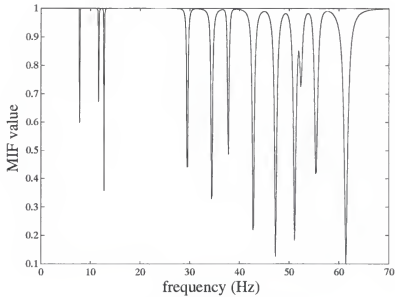


Figure 5.1 Typical MIF Plot

node point excitation locations with forces being applied in any direction at the node points. The second algorithm is a constrained version in that the direction of the excitation is constrained to be 0, 30, 45, 60, or 90 degrees in each x, y, and z plane. The constrained algorithm was developed to provide an improvement in algorithm speed by reducing the number of search points in the design space. In addition, the attachment of the excitation hardware on the structure during the modal test would be easier if the angles of orientation are limited. An outline of the GMIF algorithms follows.

Coding. The GA chooses an initial population of node points and directions for excitation location. The node points and the directions are referred to as design variables. The design variables are represented differently for the constrained and unconstrained versions of the GMIF algorithm. In both the constrained and unconstrained cases the node point locations of the excitations are treated as discrete design variables. Discrete design variables represent a finite number of variables to search over, and for this application they represent all of the node points in a FEM that are being considered as possible excitation locations. The direction design variables are two angles in spherical coordinates, α and β , which are used to calculate the direction of the force as seen in Figure 5.2. For the

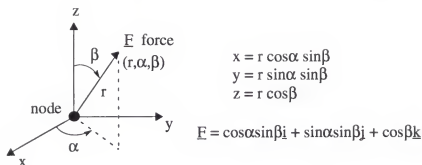


Figure 5.2 Excitation Selection by GMIF

constrained algorithm the orientation of the excitation is considered discrete in the sense that there are a finite number of angles (i.e., 0, 30, 45, 60, or 90 degrees) from which the GA selects α and β . For the unconstrained case, the angles of orientation are considered to be continuous in that the GA searches over all possible angles. For both cases the force is assigned a unit magnitude in order to only evaluate the angle of orientation of the force and not the magnitude. Table 5.1 presents a list of variables used in the GMIF selection algorithm.

Table 5.1 GMIF Design Variable Description

Unconstrained		Constrained	
<u>Design Variable</u>	<u>Type</u>	<u>Design Variable</u>	<u>Type</u>
node	discrete	node	discrete
α (any angle)	continuous	α (0,30,45,60,90 degrees)	discrete
β (any angle)	continuous	β (0,30,45,60,90 degrees)	discrete

Evaluation. The next step in the GA is to evaluate the fitness of each population member or excitation. The fitness of a member is based on the calculation of the MIF corresponding to each force that makes up a single member. All of the MIFs for a single member are assembled into a MIF matrix,

$$\text{MIF}_m = \begin{bmatrix} \text{mif}_{f1}(\omega_1) & \text{mif}_{f1}(\omega_2) & \cdots & \text{mif}_{f1}(\omega_m) \\ \text{mif}_{f2}(\omega_1) & \text{mif}_{f2}(\omega_2) & \cdots & \text{mif}_{f2}(\omega_m) \\ \vdots & \vdots & \ddots & \vdots \\ \text{mif}_{f_{nf}}(\omega_1) & \text{mif}_{f_{nf}}(\omega_2) & \cdots & \text{mif}_{f_{nf}}(\omega_m) \end{bmatrix} \begin{matrix} \text{Force 1} \\ \text{Force 2} \\ \vdots \\ \text{Force nf} \end{matrix} \quad (5.2.3)$$

$\begin{matrix} \uparrow & \uparrow & & \uparrow \\ 1^{\text{st}} & 2^{\text{nd}} & & m^{\text{th}} \\ \text{natural frequencies of interest} \end{matrix}$

Next the minimum of each column of MIF_m is taken to find the maximum drop-off values of the union of the MIFs of each force resulting in a minimum MIF vector,

$$\underline{\text{MIF}}_v = \underset{\text{minimum}}{\text{column}} (\text{MIF}_m) \quad (5.2.4)$$

The objective function is calculated as a weighted sum of the elements of $\underline{\text{MIF}}_v$,

$$J_{\text{obj}} = \sum_{i=1}^m w_i \text{MIF}_{vi} \quad (5.2.5)$$

The weights may be used to emphasize the drop-off values of particular modes. The objective function of Eq. (5.2.5) is designed to find excitation sources which exhibit sharp MIF drop-offs for as many modes as possible.

Selection, crossover, and mutation. Once the fitness of the initial population is established the population is allowed to evolve over a fixed number of generations. The information contained in the initial population is crossed over between members and sent to the next generations. Members of new generations which are more fit than the previous generation (i.e., have better drop-off values) replace the less fit members in the evolving population. Mutations that occur in the population allow for the population to remain diverse during the evolutionary process, keeping the design search space open.

5.2.2 Sensor Placement

Once an excitation source has been selected, the MIF corresponding to the chosen excitation source may be used along with a GA to locate a sensor set. First, the FRF matrix is calculated for the FEM under consideration using the chosen excitations. When the MIF is calculated to evaluate an excitation source, all DOFs of the mode shape matrix are used to

calculate the frequency response matrix, H . When the MIF is used to evaluate a sensor placement, only the sensor candidate DOF or three DOFs in case of a triax sensor set, is used to calculate the frequency response matrix, H . A MIF must be calculated for each force for a candidate sensor and the minimum MIF value for each mode is taken. The MIF values for the target modes for the i^{th} DOF are taken as the minimum MIF values for all of the forces in an excitation set,

$$\underline{\text{MIF}}_i = \underset{\text{minimum}}{\text{column}} \begin{bmatrix} - \text{MIF}_i(\text{force}_1) - \\ - \text{MIF}_i(\text{force}_2) - \\ \vdots \\ - \text{MIF}_i(\text{force}_n) - \end{bmatrix} \quad (5.2.6)$$

The MIF vector of Eq. (5.2.6) is calculated for all candidate sensor DOFs. A weighted sum of the MIF values for each DOF is made and assembled into the MIF vector,

$$\text{MIF}_v = \left\{ \begin{array}{c} \sum w\text{MIF}_1 \\ \sum w\text{MIF}_2 \\ \vdots \\ \sum w\text{MIF}_n \end{array} \right\} \quad (5.2.7)$$

where w is an $(1 \times m)$ weight vector used to emphasize MIF drop-off values. The variable n is the total number of candidate sensor DOFs for unconstrained sensor placement or the total number of candidate sensor nodes for triaxially-constrained sensor placement. Once MIF_v has been calculated, the node or dof with minimum MIF_v sum is retained as the first sensor. The MIF_v vector is recalculated using all remaining DOFs plus the single sensor chosen, and the next dof or node is chosen with minimum MIF_v value. This iterative process is performed until the desired number of sensors is chosen.

5.3 Observability and Controllability

Consider the set of discrete linear second-order differential equations of motion corresponding to a particular n DOF FEM of a structure,

$$M\ddot{\underline{x}}(t) + D\dot{\underline{x}}(t) + K\underline{x}(t) = B\underline{u}(t) \quad (5.3.1)$$

$$\underline{\dot{y}}(t) = \underline{C}\underline{\dot{x}}(t) \quad (5.3.2)$$

where \underline{M} , \underline{D} , and \underline{K} are the $(n \times n)$ mass, damping, and stiffness matrices, $\underline{x}(t)$ is the $(n \times 1)$ displacement vector, and $\underline{u}(t)$ is the $(n \times 1)$ input function of the system. The over dots represent differentiation with respect to time. By choosing

$$\underline{z}(t) = \begin{bmatrix} \underline{x}(t) \\ \underline{\dot{x}}(t) \end{bmatrix} \quad (5.3.3)$$

Eq. (5.3.1) can be rewritten in state space form as

$$\underline{\dot{z}}(t) = \begin{bmatrix} \underline{0} & \underline{I} \\ -\underline{M}^{-1}\underline{K} & -\underline{M}^{-1}\underline{D} \end{bmatrix} \underline{z}(t) + \begin{bmatrix} \underline{0} \\ \underline{M}^{-1}\underline{B} \end{bmatrix} \underline{u}(t) \quad (5.3.4)$$

or equivalently

$$\underline{\dot{z}}(t) = \underline{A}\underline{z}(t) + \underline{\hat{B}}\underline{u}(t) \quad (5.3.5)$$

where \underline{A} is the $(2n \times 2n)$ state matrix, $\underline{\hat{B}}$ is the $(2n \times o)$ input influence matrix, and $\underline{u}(t)$ is the $(o \times 1)$ input function vector. The output of the system defined by Eq. (5.3.2) may be rewritten as

$$\underline{y}(t) = \underline{\hat{C}}\underline{z}(t) \quad \text{where} \quad \underline{\hat{C}} = [\underline{C} \quad \underline{0}] \quad (5.3.6)$$

The vector $\underline{y}(t)$ is the $(l \times 1)$ system output, and $\underline{\hat{C}}$ is the $(l \times 2n)$ output influence matrix. Figure 5.3 is a pictorial representation of the matrices and vectors of a state space system of equations and describes the purpose of each.

An important consideration in the control of the system described by Eq. (5.3.4) is if the system is controllable and observable. Another consideration is the observability and controllability of the modes of the system defined by Eq. (5.3.4). Several techniques for calculating the observability and controllability of modes have been explored. One of the most common tests for controllability and observability is the Popov-Belevitch-Hautus (PBH) test (Kailath, 1980). For the purpose of vibration control, it is most common to

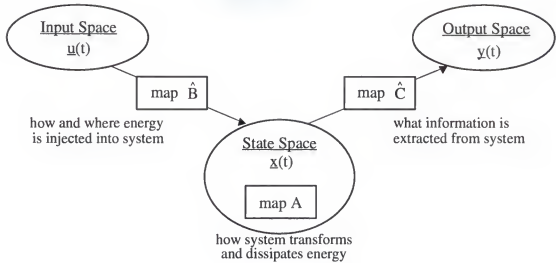


Figure 5.3 State Space Variable Description

overstep the conversion of Eq. (5.3.1) into state space form and to calculate the observability and controllability directly from Eq. (5.3.1). The PBH eigenvector test for a second-order system (Laub and Arnold, 1984) states that given the system defined in Eqs. (5.3.1) and (5.3.2):

1. The i^{th} mode will not be controllable from the j^{th} input if and only if there exist a left eigenvector \underline{q}_i such that

$$\underline{q}_i^T [\lambda_i^2 M + \lambda_i D + K] = \underline{0}^T \quad (5.3.7)$$

$$\underline{q}_i^T \underline{b}_j = \underline{0}^T \quad (5.3.8)$$

2. The i^{th} mode will not be observable from the k^{th} output if and only if there exist a right eigenvector \underline{p}_i such that

$$[\lambda_i^2 M + \lambda_i D + K] \underline{p}_i = \underline{0} \quad (5.3.9)$$

$$\underline{c}_k^T \underline{p}_i = \underline{0} \quad (5.3.10)$$

where \underline{b}_j is the j^{th} column vector of the input influence matrix, B , and \underline{c}_k is the k^{th} column vector of the output influence matrix, C .

This evaluation of controllability and observability tells whether or not the modes are completely observable or controllable; it does not address the issue of degree of observability and controllability. The issue of degree of controllability and observability is explored in a paper by Hamdan and Nayfeh (1989). In this work the matrices Q^TB and CP are used to evaluate the degree of controllability and observability of the modes of a system. The matrix Q^T is the transpose of the matrix whose columns are the m left eigenvectors of Eq. (5.3.7) and B is the output influence matrix whose columns are the o output influence vectors.

$$Q^TB = \begin{bmatrix} - & q_1^T & - \\ - & q_2^T & - \\ & \vdots & \\ - & q_m^T & - \end{bmatrix} \begin{bmatrix} | & | & & | \\ b_1 & b_2 & \dots & b_o \\ | & | & & | \end{bmatrix} \quad (5.3.11)$$

The matrix C is the output influence matrix whose l rows contain the output influence vectors and P is the matrix whose columns are the m right eigenvectors of Eq. (5.3.9).

$$CP = \begin{bmatrix} - & c_1 & - \\ - & c_2 & - \\ & \vdots & \\ - & c_l & - \end{bmatrix} \begin{bmatrix} | & | & & | \\ p_1 & p_2 & \dots & p_m \\ | & | & & | \end{bmatrix} \quad (5.3.12)$$

The (mxo) matrix Q^TB contains information about the controllability of the modes and the (lxm) matrix CP contains information about the observability of the modes. If the ij^{th} entry of Q^TB is 0 then the i^{th} mode is uncontrollable from the j^{th} input. Similarly, if the ki^{th} entry of CP is 0 then the i^{th} mode is unobservable from the k^{th} output. If the ij^{th} entry of the controllability matrix is nonzero, then what information may be gained about the degree of controllability of the i^{th} mode from the j^{th} input? The ij^{th} element of the Q^TB matrix is the vector dot product of q_i and b_j . If the two sub-spaces spanned by these vectors are parallel then the i^{th} mode is completely controllable from the j^{th} input, and if the two sub-spaces are orthogonal then the i^{th} mode is completely uncontrollable from the j^{th} input. If the two sub-spaces are neither orthogonal or parallel then the angle between the two is an indication of the degree of controllability of the i^{th} mode from the j^{th} input. This relationship is illustrated in Figure 5.4 and the magnitude of the vector dot product is,

$$|q_i^T b_j| = \|q_i\| \|b_j\| \cos \theta_{ij} \quad (5.3.13)$$

A similar argument may be made for the observability of the i^{th} mode from the k^{th} output using the magnitude of the vector dot product,

$$|c_k p_i| = \|c_k\| \|p_i\| \cos \phi_{ki} \quad (5.3.14)$$

The angle θ_{ij} is a direct measure of the degree of controllability of the i^{th} mode and ϕ_{ki} is a direct measure of the degree of observability of i^{th} mode. The degree of controllability and observability decrease as θ_{ij} and ϕ_{ki} go from 0 to $\pi/2$ as shown in Figure 5.4.

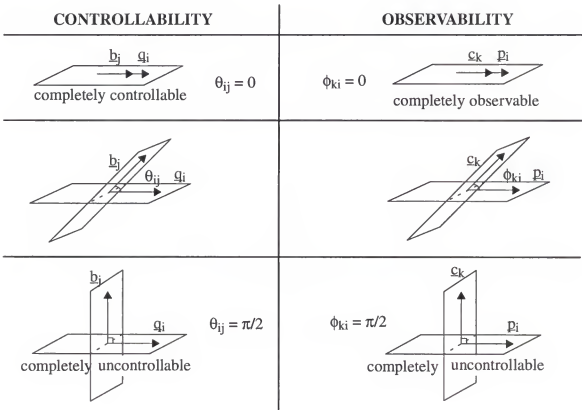


Figure 5.4 Controllability and Observability

The above argument has been made from a dynamic controls perspective. The same argument may be used to gain information about actuator and sensor placement during modal tests of a structure. Using the FEM of a particular structure the degree of

controllability of a modal test excitation layout may be used to optimally select an excitation location. Similarly, the degree of observability of a modal test sensor layout may be used to select a sensor configuration which will result in an increase in the amount of modal information obtained.

5.3.1 Excitation Placement

The degree of controllability based on the calculation of the angle between the sub-space spanned by a mode shape of the system and the sub-space spanned by the input influence vectors of the matrix of Eq. (5.3.1) is used to evaluate how effective the input $\underline{u}(t)$ may be in controlling the modes of the system. Consider that Eq. (5.3.1) is the equation of motion for a particular structure and that the right hand side, $B\underline{u}(t)$, is the force that will be applied to excite the structure for modal testing. In order to gain the most information from the modal test, an excitation location which will excite a chosen range of target modes well is required. The measure of modal controllability is an indication of how great an effect a particular input, b_j , may have on the mode shapes of the system. An input with a higher degree of controllability over a mode will be more successful in exciting that mode than an input with a lower degree of controllability over that mode. Therefore, it is proposed that the angle θ_{ij} of Eq. (5.3.13) may be used as a measure of how successful the input excitation b_j will be in exciting mode q_i . Since there are an infinite number of possible input influence vector values, an optimization technique is needed to search for an input influence vector which maximizes the controllability of the target modes. A genetic algorithm is employed as the optimization tool for this purpose.

Coding. The coding of the Genetic Controllability (GCON) Algorithm is identical to the coding of the GMIF algorithm. One design variable represents the node point locations of the forces, the other design variables represent the angle orientations of the forces in spherical coordinates as described in Figure 5.2. The difference between the GMIF and the GCON algorithms is in the fitness evaluation of the population.

Evaluation. The fitness of each population member is based on the calculation of the controllability vector. The location and orientations of each force in a population member is used to calculate an input influence vector. The j^{th} force of a member is used to calculate a portion of the input influence vector as,

$$\underline{b}_{fj} = \begin{Bmatrix} \cos \alpha_{fj} \sin \beta_{fj} \\ \sin \alpha_{fj} \sin \beta_{fj} \\ \cos \beta_{fj} \end{Bmatrix} \quad (5.3.15)$$

The unit magnitude vector \underline{b}_{fj} is calculated for all j forces of a member and assembled into the global input influence vector. The global input influence vector, \underline{b} , is initially an n DOF vector of zeros. Once the individual force unit input influences are calculated, they are placed in the global input influence vector, \underline{b} , at the DOFs of each corresponding force node point,

$$\underline{b} = \begin{Bmatrix} 0 \\ \vdots \\ \underline{b}_{f1} \\ 0 \\ \vdots \\ \underline{b}_{f2} \\ \underline{b}_{f3} \\ 0 \\ \vdots \\ \underline{b}_{fnf} \\ 0 \end{Bmatrix} \quad (5.3.16)$$

where nf is the total number of excitation devices represented in a population member. Since the magnitude of the \underline{b}_{fj} 's affect the controllability of the system, each \underline{b}_{fj} is scaled to unit magnitude so as to compare the directions of the forces as apposed to the magnitudes. The unit input influence vector is used in conjunction with the left-hand eigenvectors of Eq. (5.3.7) to calculate the $(mx1)$ degree of controllability vector from Equation 5.3.13,

$$\underline{\theta} = \begin{Bmatrix} \theta_1 \\ \theta_2 \\ \vdots \\ \theta_m \end{Bmatrix} \quad (5.3.17)$$

The i^{th} entry of the degree of controllability vector is

$$\theta_i = \cos^{-1} \frac{|\mathbf{q}_i^T \mathbf{b}|}{\|\mathbf{q}_i\|} \quad (5.3.18)$$

The entries of the $(m \times 1)$ controllability vector, $\boldsymbol{\theta}$, represents the controllability of each of the m modes of the system from the locations and directions defined by \mathbf{b} . The algorithm is designed to find excitation location which exhibit the highest degree of controllability for the modes of interest. Therefore, the most fit members of a population are forces which minimize the entries of the vector $\boldsymbol{\theta}$. Doing so minimizes the angle between the input vector sub-space and the mode shape sub-spaces thus increasing the amount of controllability and the amount of power input into the modes. The objective function is calculated as a weighted sum of the entries of $\boldsymbol{\theta}$,

$$J_{\text{obj}} = \sum_{i=1}^m w_i \theta_i \quad (5.3.19)$$

The weight may be used to emphasize the controllability of particular modes over other modes.

Selection, cross-over, and mutation. The population is allowed to evolve over a fixed number of generations as in the GMIF algorithm. The most fit members are those that minimize the objective function of Eq. (5.3.19).

5.3.2 Sensor Placement

The degree of observability of the modes of the system in Eq. (5.3.1) is based on the calculation of the angle between the modes of the system and the output influence matrix. When performing a modal test of structure, it is not likely that all DOFs in the FEM will be instrumented during the test due to cost constraints. In order to get the most information about the modes of the system, a reduced sensor set which has the greatest degree of target mode observability should be chosen. Therefore, the angle ϕ of Eq. (5.3.14) will be used as a

measure of how successful a sensor configuration is in measuring a group of chosen target modes.

There are a finite number of DOFs or sensor possibilities represented in a FEM, therefore, an optimization technique is not needed. In order to evaluate each DOF location individually, the output influence matrix, C , is set equal to an $(n \times n)$ identity matrix. Therefore, the observability of the k^{th} DOF of the i^{th} mode is obtained from Equation 5.3.15 as

$$\phi_{ki} = \frac{|P_{ki}|}{\|p_i\|} \quad (5.3.20)$$

where P_{ki} is the ki^{th} entry of the right eigenvector matrix of Eq. (5.3.12) and p_i is the i^{th} column of the right eigenvector matrix, P . If this value is calculated for all candidate DOFs and all target modes the resulting $(n \times m)$ observability matrix,

$$\Phi = \begin{bmatrix} \phi_{11} & \phi_{12} & \cdot & \cdot & \phi_{1m} \\ \phi_{21} & \phi_{22} & \cdot & \cdot & \phi_{2m} \\ \cdot & \cdot & & & \cdot \\ \cdot & \cdot & & & \cdot \\ \cdot & \cdot & & & \cdot \\ \phi_{n1} & \phi_{n2} & \cdot & \cdot & \phi_{nm} \end{bmatrix} \quad (5.3.21)$$

The rows of the observability matrix represent DOFs and the columns represent the modes. Once the observability matrix has been calculated, the DOFs for sensor location must be evaluated. The observability column corresponding to each mode is sorted, and the DOFs with the minimum ϕ values (i.e., greatest observability) for each mode are selected as sensor locations.

CHAPTER 6

PRE-MODAL TEST PLANNING ALGORITHM APPLICATION: NASA EIGHT-BAY TRUSS

6.1 Introduction

The NASA 8-bay truss is used to compare the techniques discussed in Chapters 4 and 5 in placing sensors and actuators for modal testing and system identification purposes. The kinetic energy, average kinetic energy, eigenvector product, driving point residue, and controllability techniques are used to place three excitation devices on the truss. A numerical simulation is performed to evaluate the effectiveness of each technique to excite the first five target modes of the structure. A cross-orthogonality check between the identified and finite element modes is performed in addition to a frequency match comparison. Effective independence, kinetic energy, average kinetic energy, eigenvector product, and observability techniques are used to place sensors on the 8-bay truss, in order to best identify the first five modes of vibration. The structural response of the truss is numerically simulated and measured at those DOFs corresponding to the sensor locations obtained using the various techniques. The eigensystem realization algorithm (ERA) is then used to evaluate the effectiveness of each sensor set with respect to modal parameter identification (Juang and Pappa 1985). A set of three hundred random sensor locations are compared to the five sensor location techniques. The cost effectiveness of each of the excitation and sensor selection techniques is evaluated.

6.2 NASA Eight-Bay Test Bed

The NASA eight-bay truss, pictured in Figure 6.1, is modeled with 96 DOFs and is considered to be lightly damped. Using the FE mass and stiffness matrices supplied by

NASA, the FE mode shapes and frequencies were calculated. When the true modal tests were performed on the truss, it was assumed that the first five modes were successfully identified (Kashangaki, 1992). Table 6.1 list the first five frequencies and mode descriptions.

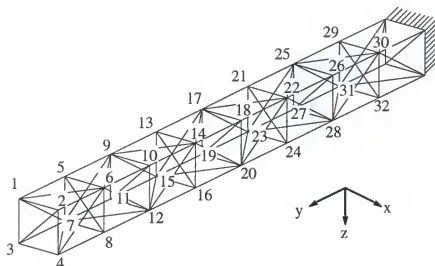


Figure 6.1 NASA 8-Bay Truss

Table 6.1 Eight-Bay Truss Frequencies and Mode Description

Mode	Frequency (Hz)	Description
1	13.925	1 st y-x bending
2	14.441	1 st y-z bending
3	46.745	1 st torsional
4	66.007	2 nd y-x bending
5	71.142	2 nd y-z bending

6.2.1 Excitation Placement

Kinetic energy, average kinetic energy, eigenvector product, driving point residue, and controllability techniques are each used to place three excitation devices on the 8-bay truss to best excite the first five modes of the structure. The excitation locations for the five techniques are pictured in Figure 6.2. The kinetic energy technique placed two excitation

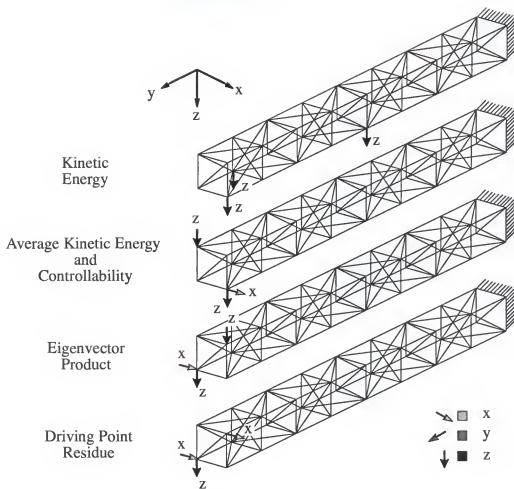


Figure 6.2 Eight-Bay Excitation Locations

sources towards the cantilevered end of the truss and one towards the center of the truss. The other four techniques clustered all of the excitation sources at the cantilevered end of the truss. It is interesting to note that the kinetic energy technique put all excitation sources in the z-direction. The remaining four techniques placed excitation sources in both the x and z directions, in addition to clustering two of the sources at a single node. The average kinetic energy and controllability techniques placed the excitation devices in the same location as seen in Figure 6.2. In a true modal test, the two excitation sources which were placed at a single node could be combined into one excitation source at that particular node in the xz-direction, thus reducing the number of excitation sources needed. The kinetic energy placement could not result in this option.

Once the excitation sources have been determined using the five techniques, the truss's response to an impulse at the chosen excitation locations is numerically simulated for the first five modes and 5% noise is added to the response data. The response, measured at all 96 DOFs to fully evaluate the effectiveness of the each excitation placement, is sampled for a length of 2 seconds at 200 Hz. Five percent noise is added to the response which is sent to ERA for system identification. A comparison of the measured frequencies and cross-orthogonalities of the identified and FE models is calculated for each excitation placement.

The five excitation placement techniques were all successful in exciting the structure at the target frequencies based on the comparison of the original FE and identified frequencies and mode shape. All of the techniques had excellent matching between identified and FEM frequencies with differences much lower than the industry standard of 5% (Flanigan and Hunt, 1993). A Frequency Response Function (FRF) is plotted for each of the excitation devices in Figure 6.3. The cross-orthogonalities between identified and FEM mode shapes for the five excitation placement techniques are pictured in Figure 6.4. All off-diagonal terms for each of the excitation sets are less than or equal to 0.02, which is well within the industry standard of ≤ 0.02 off-diagonals for primary modes (Flanigan and Hunt, 1993).

Of the five techniques, the cross-orthogonality of kinetic energy was worst although it was well within the acceptable range of off-diagonal values. The cross-orthogonality of average kinetic energy, controllability, eigenvector product, and driving point residue techniques had similar values; all of the off-diagonal elements for each of the techniques were ≤ 0.01 . Recall that kinetic energy placed all excitation sources in the z-direction at three separate nodes, and that the other three location techniques placed excitation sources in both the x and z directions and collocated two sources at one node. The similar placement configurations at the cantilevered tip of the truss resulted in similar cross-orthogonalities. Based on the frequency matching and cross-orthogonality between identified and FEM frequencies and mode shapes, and on the FRFs, each of the five excitation location

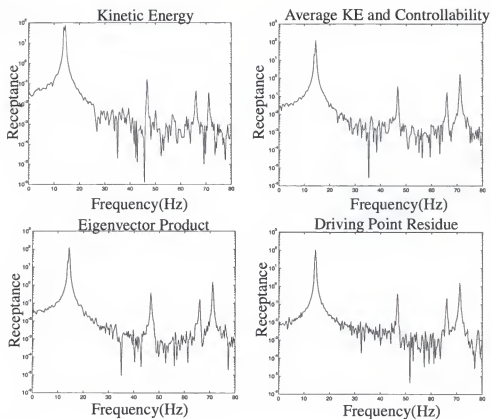


Figure 6.3 Eight-Bay Excitation Location Frequency Response of Time Domain Data

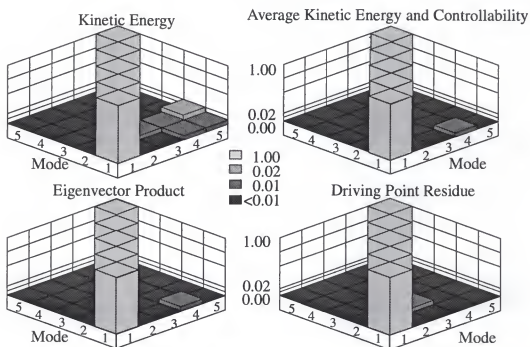


Figure 6.4 Eight-Bay Excitation Placement Cross-orthogonality of Identified and FEM Modes 1 to 5

techniques identified an acceptable three point excitation location for exciting the first 5 modes of the 8-bay truss.

6.2.2 Sensor Placement

Using the FE modes and frequencies, the five sensor placement techniques, effective independence, kinetic energy, average kinetic energy, eigenvector product, and observability were assigned the task of best identifying the first 5 modes of vibration by placing 15 sensing devices on the truss. The five sensor set configurations are pictured in Figure 6.5. Each of the techniques clustered the sensors in two locations on the truss at the cantilevered end and at the midspan. Effective independence, average kinetic energy, and eigenvector product techniques collocated fourteen of the fifteen sensors at seven node points. The kinetic energy technique collocated twelve of the fifteen sensors at six node points and observability collocated eight sensors at four node points. From a cost standpoint, the collocation of as many sensors as possible is desired. None of the five techniques placed sensors in the y DOF. This is to be expected since the first five modes do not include significant motion in the y -direction.

The simulated response, with 5% noise added, obtained using the excitation configuration determined from the average kinetic energy technique was used to test the sensor sets. The exact same response was used to test each sensor configuration, by taking from the 96 DOF response only those DOFs corresponding to the sensor locations to be evaluated. The response data of each sensor set were sent to ERA for frequency and mode shape identification.

The excitation placement found using the average kinetic energy technique is used to excite the structure to test the various sensor locations. Each of the five sensor placement techniques measured the target frequencies well as can be seen from the percent difference in the FE and identified frequencies given in Table 6.2. The 96 DOF FEM mass matrix was reduced to a 15 DOF mass matrix using exact reduction and the cross-orthogonality between

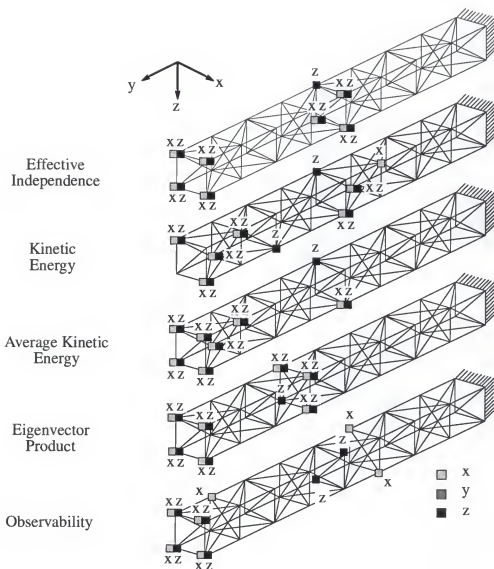


Figure 6.5 Eight-Bay Sensor Locations

identified and FEM modes 1 through 5 was calculated using the reduced mass matrix. The cross-orthogonality for each of the sensor sets is given in Figure 6.6.

For each of the five cases the cross-orthogonality terms were within acceptable limits. The off-diagonal terms corresponding to the primary modes were all ≤ 0.02 . Effective independence, kinetic energy, and eigenvector product techniques resulted in similar cross-orthogonalities (all off-diagonals are ≤ 0.01). Observability technique gave the worst cross-orthogonality results of the five techniques even though the off-diagonal elements

remained within acceptable values. The improved performance of the effective independence, kinetic energy, observability, and eigenvector product techniques over the average kinetic energy technique can clearly be seen in the next section when the five techniques are compared to the random sensor sets.

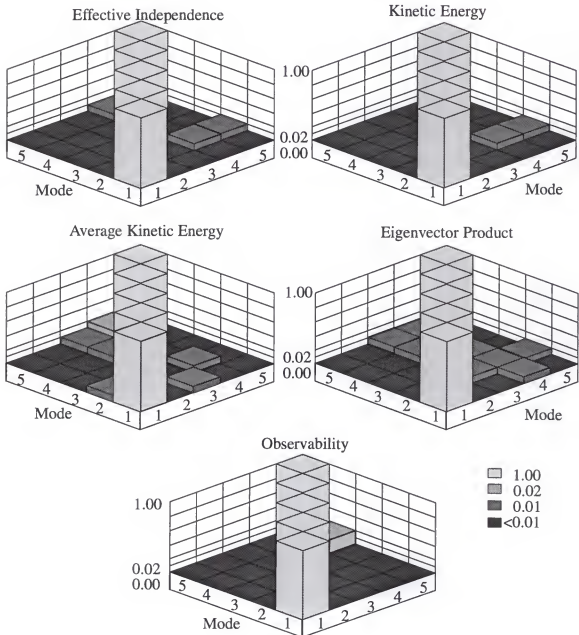


Figure 6.6 Eight-Bay Sensor Placement Cross-orthogonality of Identified and FEM Modes 1 to 5

Table 6.2 Percent Difference in FE and Identified Frequencies

MODE	EI	KE	AKE	EVP	CON
1	0.042	0.052	0.066	0.042	0.17
2	0.018	0.004	0.012	0.018	0.19
3	0.141	0.036	0.013	0.142	0.30
4	1.140	0.032	0.455	1.140	0.79
5	0.021	0.008	0.037	0.021	0.15

6.2.3 Results: Random Sensor Location

Three hundred random sets of 15 sensors each were generated and evaluated in order to assess the level of increased performance of the various sensor placement algorithms against pure chance. The same time domain response with 5% noise used in the previous section was partitioned to the random sensor configurations. For the time domain data of each sensor set, ERA is used to identify the first five frequencies and mode shapes. The cross-orthogonalities and frequency differences between the identified and FEM modes and frequencies were calculated. Figure 6.7 is a comparison of cross-orthogonalities for the 300 random sensor sets and for the five sensor placement techniques (EI, KE, AKE, EVP, and OBS). The bar portion of each graph corresponds to each random sensor set value and the straight lines correspond to the five evaluated sensor configurations (EI, KE, AKE, EVP, and OBS) and to the average value of all the random sensor sets (ARS). The top graph of Figure 6.7 is a plot of the maximum off-diagonal elements of the cross-orthogonality matrix, the center graph is the average off-diagonal of the cross-orthogonality matrix, and the bottom graph is the two norm of the cross-orthogonality matrix minus the identity matrix.

In general, the average random sensor set was within the acceptable limits on frequency matching and cross-orthogonality. This is due to the fact that a large number of sensors were placed on the truss and approximately 1/3 of the trusses node points would be instrumented by the random sensor sets. Statistically, the random sets would have good chances of capturing pertinent modal information. Of the five techniques evaluated, kinetic energy,

effective independence, eigenvector product, and observability gave better results than 97% of the random sets as can be seen in Figure 6.7. The maximum off-diagonal and the average off-diagonal of the cross-orthogonality matrices of the three techniques are less than those for the average random set. In addition the two norm of the difference between the cross-orthogonality and the identity matrix for the three techniques is lower than that of the average random set. However, the average kinetic energy gave results similar to the average random configuration, and showed little to no improvement over the purely random placement of fifteen sensors. The maximum off-diagonal of the AKE set was larger than that for the average random set and the average off-diagonal and two norm were approximately equal to those of the average random set.

6.3 Computational Efficiency

For this particular example, the results for each of the excitation and sensor placement techniques are all relatively comparable. The targeted modes and frequencies are excited by all of the excitation placements and properly identified by all of the sensor sets evaluated. This is illustrated by the acceptable differences in FEM and identified frequencies and cross-orthogonality values. The agreement between all the techniques can be partially contributed to the fact that the “the modal test” was a numerical simulation. The differences in the results for excitation evaluation and identification may be greater for a true modal test. However, an important issue that must be considered when using the discussed techniques for excitation and sensor location is the computational cost of each evaluation versus the accuracy of the modal test results. As can be seen from Table 6.3, the most efficient technique for excitation and sensor location is the eigenvector product technique. It may well be that on a more complicated example, the more computationally efficient techniques may result in modal test configurations which give less accurate modal information than the more complex placement techniques. A larger system model with more DOFs may make the

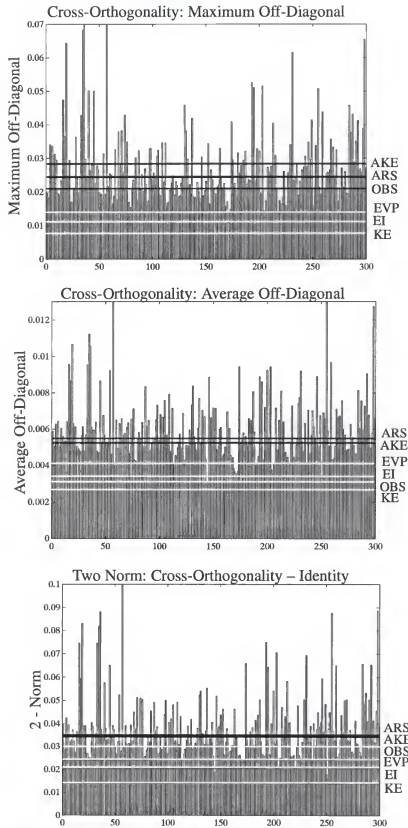


Figure 6.7 Eight-Bay Cross-Orthogonalities of Five Techniques Compared to 300 Random Sensor Sets

tradeoffs between the computational cost of placement and the accuracy of the modal identification more apparent.

Table 6.3 Total Floating Point Calculations for Each Placement Technique

Technique	Total flop count	Placement
EI	812,000	sensors
KE	92,700	sensors & excitation
AKE	93,200	sensors & excitation
EVP	480	sensor & excitation
DPR	7,600	excitation
CON	7,600	excitation
OBS	7,600	sensor

6.4 Conclusion

Based on the evaluation of the numerical simulation, each of the five excitation techniques successfully placed three excitation sources on the structure which would excite the first five modes of vibration. The sensor placement techniques of effective independence, kinetic energy, eigenvector product, and observability found sensor locations which showed better frequency matching and cross-orthogonality than 97% of the random sensor sets. The sensor set obtained using average kinetic energy showed no improvement in cross-orthogonality or frequency matching over those of the random sensor sets. Based on the similar results of the placement techniques for sensors and actuators, a more complex structure will now be used to compare the techniques discussed in this chapter as well as other techniques outlined in Chapter 5.

CHAPTER 7

PRE-MODAL TEST PLANNING ALGORITHM APPLICATION: MICRO-PRECISION INTERFEROMETER TRUSS

7.1 Introduction

A comparative study of several pre-modal test planning techniques is presented using the Jet Propulsion Laboratories' Micro-Precision Interferometer (MPI) testbed. Mode indicator functions calculated using a reduced FEM of the structure and degrees of target mode controllability are used in conjunction with genetic algorithms to find location and orientation of two excitation sources in order to optimally excite a chosen range of target modes during a modal test. Effective independence, kinetic energy, eigenvector product, observability, and mode indicator function techniques are used to place a combination of sensors on the structure for the purpose of modal identification. The sensors are placed in two ways: independent sensor placement and triaxially constrained placement. A numerical simulation of the response of the structure is used to evaluate the effectiveness of each of the placement techniques to identify the target modal parameters of the structure. The effect of FEM error on the various placement techniques is evaluated.

7.2 Micro-Precision Interferometer Test Bed

The MPI, shown pictorially in Figure 7.1, is a testbed that has been built in order to study structural control systems in the development of space interferometers. Modal tests were performed on the MPI structure by two independent groups (Sandia National Laboratories and the Jet Propulsion Laboratories (Red-Horse et al., 1993; Carne et al., 1993; Levine-West et al., 1994).

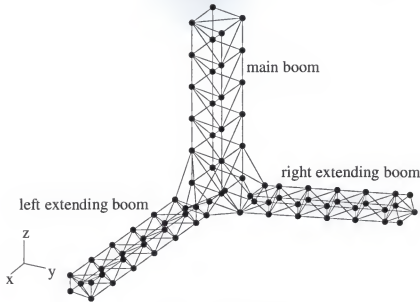


Figure 7.1 MPI Structure

The FEM used to evaluate the placement techniques in the current work was obtained from Sandia National Laboratories (Red-Horse et al., 1993). The model used is a 240 DOF Guyan-reduced FEM which has been updated using the data obtained from the modal test of the structure. The 240 DOFs correspond to three DOFs (x, y, z) at each of the 80 node balls. The frequencies from the Guyan-reduced FEM corresponding to the first 12 non-rigid-body modes are given in Table 7.1 and are compared to actual frequencies obtained during the modal test.

7.3 Excitation Placement

During the original modal test of the MPI structure, two excitation sources were used as pictured in the top portion of Figure 7.2. The lower portion of this figure is the excitation configurations that were obtained by optimizing the MIFs of the FEM using a GA (GMIF) and by optimizing the modal controllability of the FEM using a GA (GCON). Both the original and the GMIF excitation locations have an exciter on the two extending booms although they are oriented differently. The GMIF set-up moves the excitation of the right extending boom to an interior point in comparison to the original configuration. The GCON

technique placed an exciter at the mid-point of the left extending boom and an exciter at the top of the main boom. Figure 7.3 gives typical frequency responses for the two excitations of the three techniques shown in Figure 7.2; the responses are measured at the sensor location shown in Figure 7.2 in the y-directions. The straight line corresponds to the first force located by each technique and the dotted line corresponds to the second.

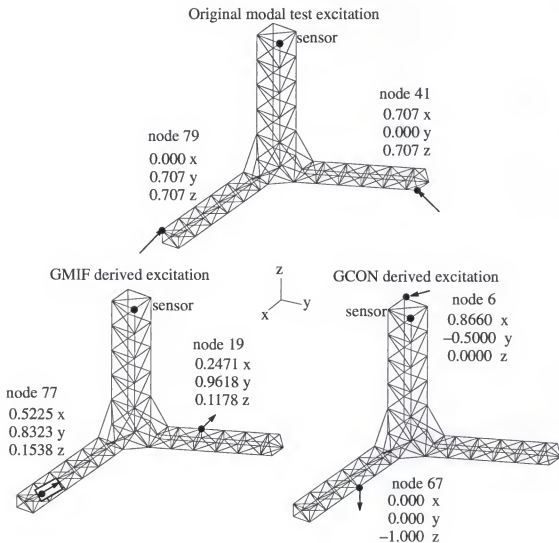


Figure 7.2 Excitation Placement on MPI Structure

Table 7.1 Reduced MPI FEM Frequencies Compared with MPI Modal Test Frequencies

Mode	Frequency (Hz) FEM	Frequency (Hz) Modal Test
1	7.82	7.75
2	11.66	11.65
3	12.75	12.67
4	29.52	29.36
5	34.45	34.06
6	37.76	37.34
7	42.81	42.25
8	47.30	46.04
9	51.14	50.69
10	52.36	53.00
11	55.41	56.82
12	61.40	60.04

The excitation devices placed by the GMIF algorithm were selected to minimize an objective function which was dependent on the MIF of each of the two excitation locations. The MIF will be nearly 1.0 except near normal modes, at which point it drops off considerably. This drop-off indicates that the mode is well excited. Therefore, it is desirable to find two excitation sources (location and orientation) which exhibit a sharp drop at all of the normal frequencies. The GMIF objective function was designed to find an excitation source(s) which exhibits sharp drop offs at normal frequencies as discussed in Chapter 5. The GCON algorithm, as discussed in Chapter 5, was designed to find excitation sources which minimize the angles between the input influence vector subspace and the sub-spaces spanned by the modes of the system thus maximizing the controllability of the modes of the structure. By choosing excitations with maximum FE modal controllability, the amount of energy being imparted to the FE modes of the system by the excitation is theoretically maximized. In order to compare the three excitation sources, the MIF drop off values for the first twelve modes of each of the excitations is calculated and shown in Table 7.2. The sharpest drop-off value for each of the modes is highlighted in bold in the table.

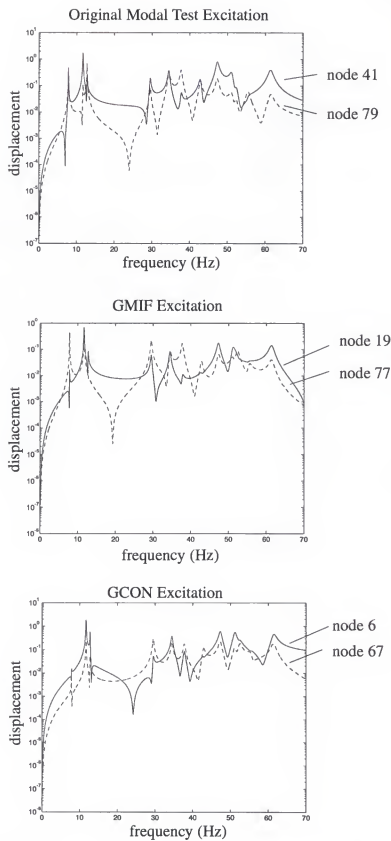


Figure 7.3 Typical Frequency Response for MPI Structure

Table 7.2 Original, GMIF, and GCON Excitation Locations MIF Values

MODE	Original		GMIF		GCON	
	41	79	19	77	6	67
1	0.0014	0.0006	0.0003	0.0106	0.0345	0.0129
2	0.0063	0.2601	0.0105	0.0048	0.0095	0.0079
3	0.0394	0.0022	0.4106	0.0428	0.0211	0.0256
4	0.0854	0.2017	0.0228	0.0706	0.4023	0.0287
5	0.0236	0.0420	0.0836	0.0184	0.0174	0.0408
6	0.4636	0.0609	0.0393	0.6855	0.2495	0.0862
7	0.0484	0.0489	0.0911	0.7126	0.6753	0.0372
8	0.0755	0.3263	0.3318	0.0644	0.0996	0.1947
9	0.1537	0.7790	0.7521	0.0824	0.0550	0.5615
10	0.7228	0.8957	0.1674	0.8050	0.7625	0.2260
11	0.4077	0.0407	0.0826	0.2747	0.4372	0.0747
12	0.0724	0.8088	0.4408	0.0591	0.0703	0.2013
min MIF	2 / 12		7 / 12		3 / 12	

The GMIF excitations exhibit a sharper drop-off than the original excitations' MIFs for 10 of the 12 target modes. The GCON exhibit a sharper drop-off than the original excitation for 6 of the 12 modes. Comparing all three techniques, the GMIF had the most minimum drop-off values at 7 followed by the GCON technique at 3, and the original excitation at 2. This is not a surprise since the GMIF is designed specifically to find excitation sources which exhibit the greatest drop-offs. An improvement in the drop-off of the GMIF excitation over the original excitation can especially be seen for the tenth mode.

It is interesting to note that even though the GMIF has the best overall MIF drop-off values, the minimum drop-off values of the GCON excitations are well within acceptable levels. The highest minimum value for the GCON technique is 0.25 for the fifth mode. However, in the next chapter it will be shown that an excitation with good controllability values does not necessarily have acceptable MIF values. In order to evaluate the performance of the genetic algorithm for excitation placement, a set of 500 random 2-point

excitations is generated. The number of random excitations, 500, was chosen because the GMIF algorithm evaluated approximately 400 population members in the search for the chosen GMIF excitation. The MIF values for each of the random excitations are calculated, sorted and graphed in Figure 7.4 and the controllability angles for the random excitations are calculated, sorted, and graphed in Figure 7.5.

The top graph of Figure 7.4 shows the maximum MIF value for the original, the GMIF derived, and the GCON derived excitations superimposed on the graph of 500 random designs in order to compare the values. The top portion shows the GMIF excitation has a smaller maximum MIF than 97% of the random population. The bottom portion of Figure 7.4 is a graph of the genetic MIF excitation placement algorithm objective function values of the random and selected excitations. An optimal excitation according to the GMIF objective function is one which has as small as possible maximum MIF drop off value. The bottom portion of the figure shows that the GMIF excitation outperformed 100% of the random population. This shows that the genetic algorithm was successful in finding a good excitation based on the objective function designed in a more computationally efficient manner than an exhaustive search.

The same evaluation was performed for the controllability angle calculations as pictured in Figure 7.5. The controllability excitation placement algorithm objective function is designed to find excitations which have a minimum controllability angle sum over the target modes to be excited. Even though the original and GMIF excitations have a smaller maximum controllability angle as seen in the middle graph of Figure 7.5, the GCON excitation has a better angle sum as seen in the bottom graph. In fact, the GCON excitation and the original excitations outperform 100% of the randomly generated excitations.

Numerical simulations of the MPI structural response to simultaneous impulses applied at the two excitation locations were calculated within the MATLAB environment. Five percent noise was added to the simulated time responses of the structure. These time responses were used along with the Eigensystem Realization Algorithm (ERA) to identify

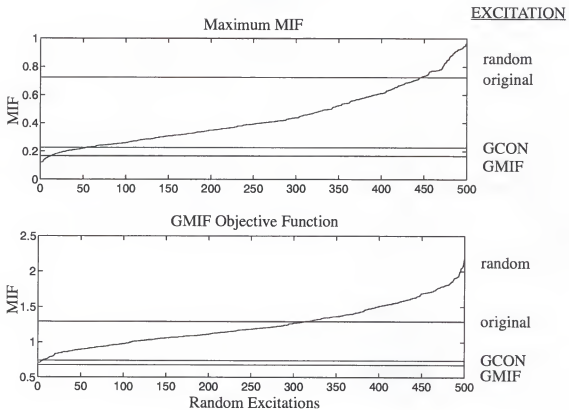


Figure 7.4 Comparison of Selected Excitation and Random Excitation MIF Values

the twelve target mode shapes and frequencies (Juang and Pappa, 1985). The evaluation of the success of ERA to identify the frequencies and mode shapes was based on a frequency percent difference comparison between identified and FE frequencies and on a cross-orthogonality check between FE and identified mode shapes using an exactly reduced mass matrix. The reduction is exact in the sense that the frequencies and mode shapes of the reduced system match exactly their counterparts in the unreduced model (O'Callahan et al., 1989).

When ERA was used to identify system mode shapes and frequencies, it missed the fifth and tenth frequencies and mode shapes when the original 41/79 DOF excitation locations were used to numerically simulate structural excitation. To illustrate this, the cross-orthogonality between FEM and ERA identified mode shapes was calculated, and is

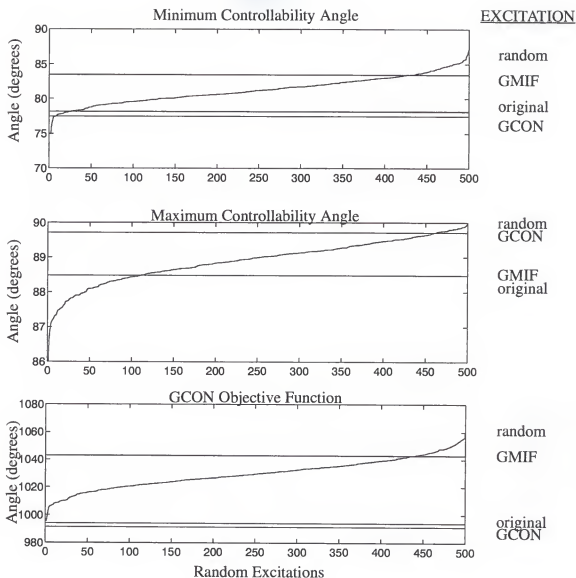


Figure 7.5 Comparison of Selected Excitation and Random Excitation Controllability Angles

pictured in Figure 7.6. For this example, the 240 DOF simulated response was partitioned to the sensor configuration obtained using the EI technique as discussed in the following section. These poor cross-orthogonality results are corroborated by the frequency response function shown in Figure 7.3 in which poor excitation can be seen for modes 5 and 10. The GMIF and GCON derived excitations resulted in successful ERA identification of all 12 mode shapes and frequencies of the original FEM.

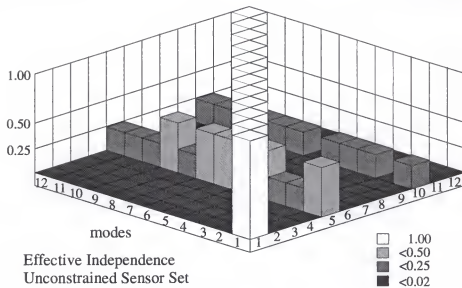


Figure 7.6 Cross-Orthogonality Between FE Modes and Identified Modes

7.4 Sensor Placement

Six sensor selection techniques, effective independence, kinetic energy, average kinetic energy, eigenvector product, observability, and MIF were used to place sensors on the MPI structure. Most of these techniques were previously evaluated for sensor placement using the NASA eight-bay testbed in Chapter 6. In that study, the five techniques of effective independence, kinetic energy, average kinetic energy, eigenvector product, and observability, performed equally well. This could be due to two reasons: (i) the structure lacked significant dynamic complexity required to distinguish between the methods or (ii) the methods were actually so similar that they led to similar results regardless of structural dynamics. One purpose of this study is to again evaluate the five techniques on a more complex dynamic system in addition to evaluating the efficacy of using the MIF for sensor placement. The second purpose is to investigate the suitability of the techniques when the sensors are constrained to be placed in a triaxial fashion.

Eighteen sensors were placed in two different studies using the six techniques in order to best identify the 12 target FEM mode shapes and frequencies. First, the techniques were used to choose 18 of the 240 DOFs as sensor locations. In the second study, the techniques were

constrained to choose 18 triaxially constrained sensors (i.e., 6 triax-sensor sets). The excitations selected using the GMIF discussed in the previous section were used to excite the MPI structure numerically in order to test the various sensor configurations.

7.4.1 Unconstrained Sensor Placement

The first placement study evaluated the six techniques' placement of 18 sensors on the MPI structure at any of the 240 DOFs (x, y, z of the 80 node balls). The first 12 flexible modes of vibration were chosen as the target modes for each technique. The locations of the sensors obtained using each of the techniques are pictured in Figure 7.7.

All of the techniques evaluated placed a majority of the 18 sensors at the ends of the three booms. In addition all of the techniques except MIF placed sensors in the two DOFs for each boom which exhibited the greatest range of motion (i.e., xy for the primary boom, xz for the extending right boom and yz for the extending left boom). The EVP technique clustered all 18 sensors at the boom tips, and the AKE techniques clustered 17 of the 18 sensors at the boom tips, with one sensor being placed near the mid-span of an extending boom. The KE technique placed 15 sensors at the boom tips with 3 sensors near the mid-span of the two extending booms. The EI technique placed 13 sensors at the boom tips and at least one sensor near the mid-span of the main and extending booms. The observability technique placed 17 of the 18 sensors at the boom tips and 1 sensor at the mid-span of an extending boom. The MIF technique resulted in the most unusual sensor configuration with several sensor being placed in the z -direction on the main boom. The z -direction is not the primary direction of motion for this portion of the truss.

Of the twelve target modes shapes, modes 2 through 11 exhibit a bending mode similar to that of second-mode-cantilevered-beam bending in at least one of the main or extending booms. Second-mode bending is clearly exhibited by the two extending booms for all target modes and is exhibited by the main boom for some of the twelve target modes. The sensor configurations chosen by the EI and KE techniques are particularly suited to capture this

second-bending mode shape due to their placement of some sensors at mid-spans of the three booms.

The FEM of the MPI structure was used with MATLAB to simulate a time response of the structure to an impact applied at the GMIF chosen excitation locations for all 240 DOFs. Five percent uncorrelated noise was added to the time response. The noisy response was then partitioned to each of the six sensor sets and was sent to ERA for mode shape and frequency identification.

All the techniques resulted in percent frequency difference between FEM and identified frequencies of much less than 1% which is well within industry accepted standards (Flanigan and Hunt, 1993). Cross-orthogonalities between FEM and identified mode shapes were calculated for each of the techniques and are pictured in Figure 7.8. In order to calculate the cross-orthogonalities, the 240 DOF FE mass matrix was reduced to 12 DOFs using exact reduction. For this size model, exact reduction was computationally acceptable, therefore, it was used to get the best cross-orthogonality comparison.

All of the off-diagonal elements of the cross-orthogonality matrix for the EI technique are within the industry accepted standards of <0.02 for primary modes (Flanigan and Hunt, 1993). This can be seen graphically in Figure 7.8. For the KE, AKE, and MIF techniques, almost all of the off-diagonal elements are <0.02 . Some of the entries are between 0.02 and 0.1 which is within the industry standard for secondary modes (<0.1). The OBS technique resulted in the most modes having cross-orthogonalities <0.10 which is acceptable for secondary modes. The 8th mode was not successfully identified by the OBS sensor set. The cross-orthogonality for the EVP technique was poor for all target modes. The cross-orthogonality of the EVP technique was evaluated with no noise, 1%, 2%, and 5% noise added to the time response. Of the four time responses evaluated, only the response with no noise gave acceptable cross-orthogonality values. Based on these calculation, the EVP technique was unsuccessful in finding an acceptable sensor set.

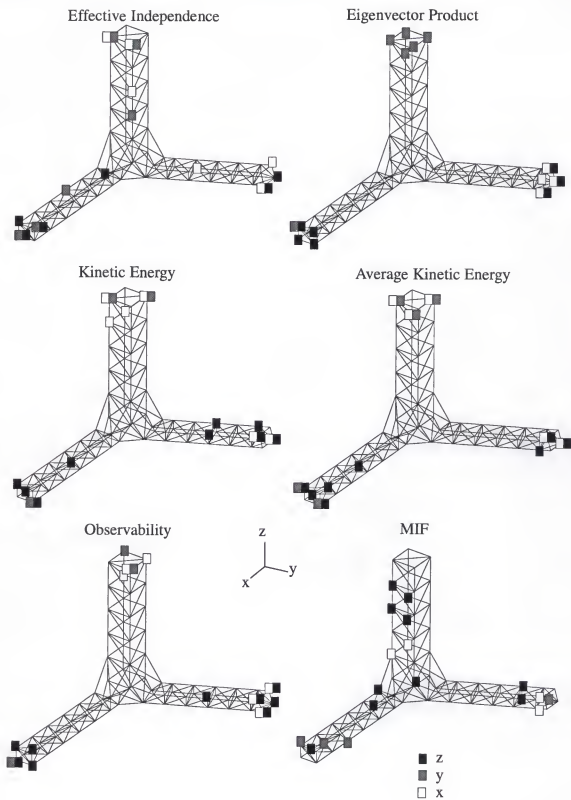
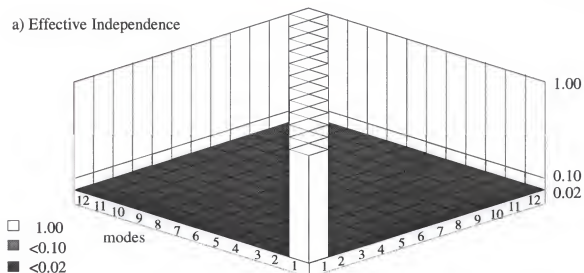
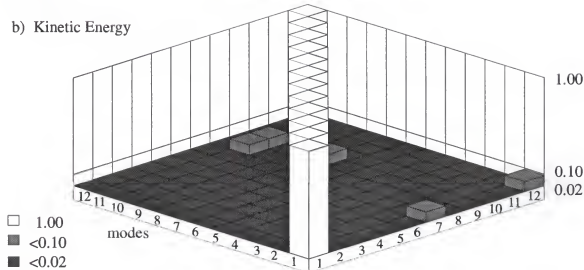


Figure 7.7 Unconstrained MPI Sensor Sets

a) Effective Independence



b) Kinetic Energy



c) Average Kinetic Energy

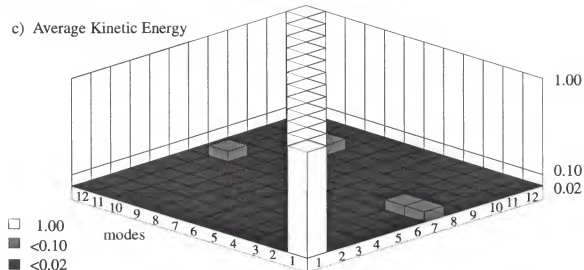
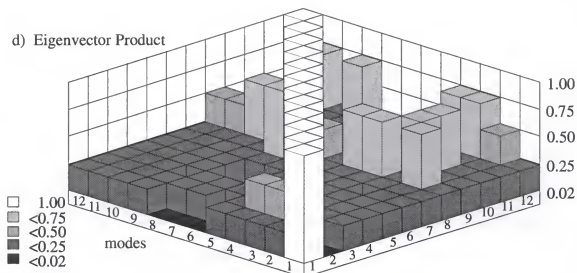
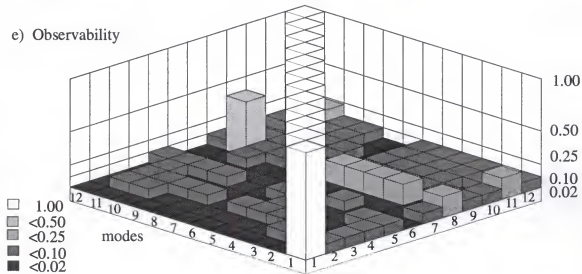


Figure 7.8 Cross-Orthogonality Between MPI FE and Identified Modes
18 Unconstrained Sensors

d) Eigenvector Product



e) Observability



e) MIF

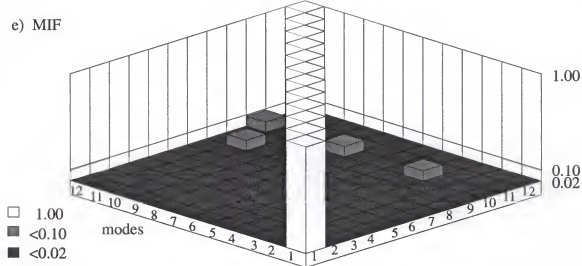


Figure 7.8 — continued

7.4.2 Triaxially Constrained Sensor Placement

The six sensor placement techniques were modified to place 6 triaxially constrained sensor sets (18 total sensors) at any of the 80 node balls of the MPI structure. The resulting 6 triax-sensor sets placed using the six placement techniques are pictured in Figure 7.9. The EI, KE, and AKE techniques grouped two sensor sets at or near the end of each boom, the OBS technique put one, two, and three sensors at the end of each boom, and the EVP technique placed three triax-sets at the ends of only two of the booms. It should be noted that if the EVP placement task were extended to placing 7 triax-sets, the seventh set would be placed at the end of the main boom using the EVP technique. The MIF sensor placement technique put two sensors at the end of the right boom, one sensor at the end of the left boom, one sensor at the base of the left boom, and two sensors on the main boom. As in the case of the unconstrained set, the MIF technique did not place any sensors on the tip of the main boom.

The time response of the MPI structure excited by the GMIF actuator locations was partitioned to those DOFs corresponding to the six triax sensor locations chosen by the six placement techniques. The partitioned numerical data with noise added was sent to ERA in order to evaluate the effectiveness of each of the triax-sensor sets in identifying the system mode shapes and frequencies. All the techniques resulted in percent frequency difference between FEM and identified frequencies of much less than 1% which is well within industry accepted standards. The cross-orthogonality calculations between the FEM target modes and the ERA identified modes were performed using an exactly reduced mass matrix as in the previous section, and are shown in Figure 7.10. All of the off-diagonal cross-orthogonality values for the KE techniques, shown in Figure 7.10, were within the industry standard of <0.02 for off-diagonal elements for primary modes.

The EI, AKE, and MIF techniques resulted in cross-orthogonalities which were within this standard for most of the modes, but which were slightly above the off-diagonal standard for a few modes. The OBS technique resulted in acceptable cross-orthogonalities for most

modes and acceptable secondary cross-orthogonalities for modes 7 through 10. The EVP technique resulted in poor off-diagonal cross-orthogonality values for all modes.

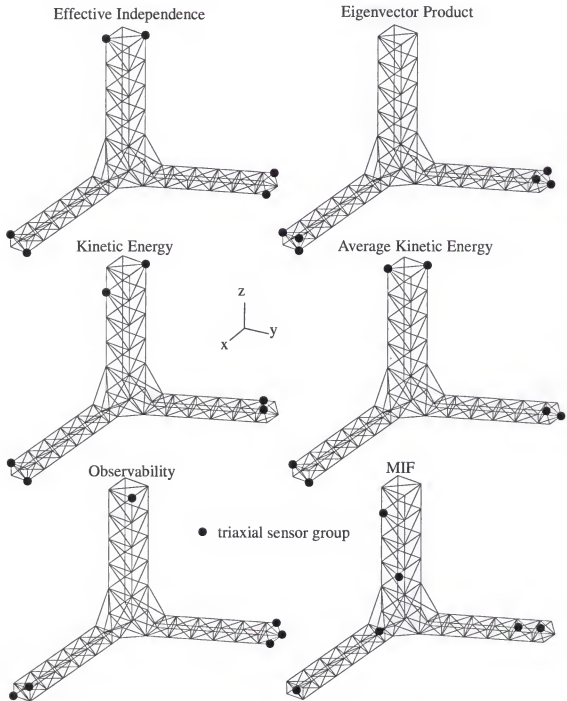
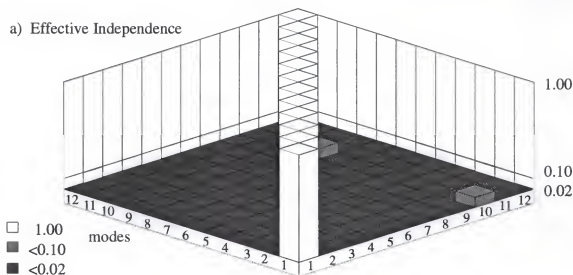
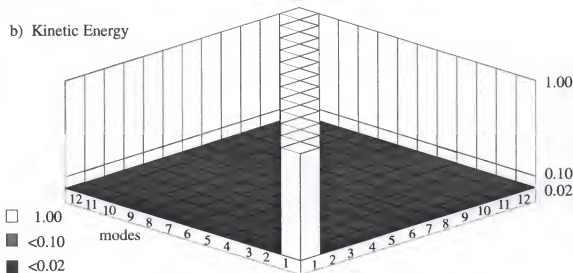


Figure 7.9 Triaxially Constrained MPI Sensor Sets

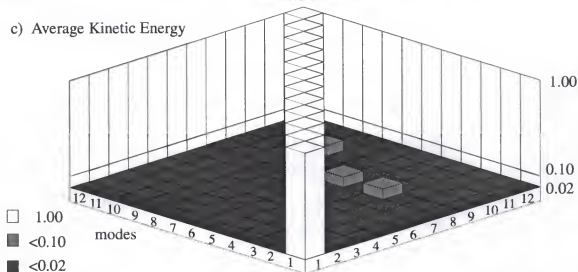
a) Effective Independence



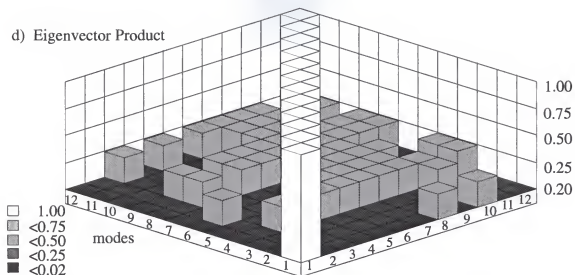
b) Kinetic Energy



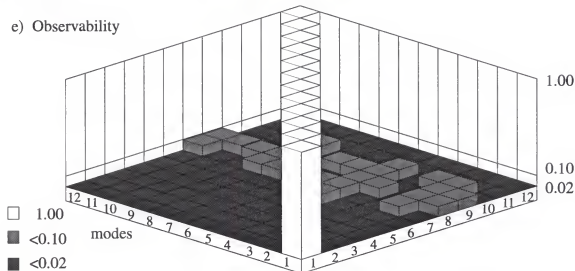
c) Average Kinetic Energy

Figure 7.10 Cross-Orthogonality Between MPI FE Modes and Identified Modes
6 Triaxially Constrained Sensors

d) Eigenvector Product



e) Observability



f) Mode Indicator Function

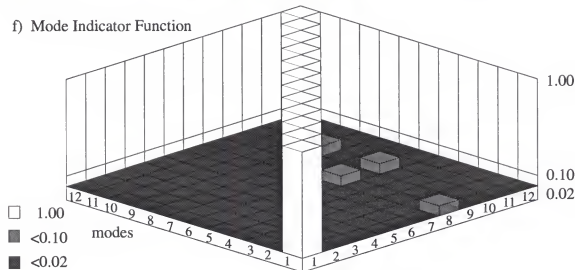


Figure 7.10 — continued

7.4.3 Unconstrained vs. Triaxially-Constrained Sensor Sets

Based on the cross-orthogonalities and frequency differences between FE and identified mode shapes and frequencies the EI, KE, AKE, and MIF techniques located sensor sets for the unconstrained and constrained examples which were successful in identifying the target mode set. Only a few of the cross-orthogonalities were slightly above acceptable primary mode values, and all values were within secondary mode standards. For the unconstrained sensor set, the EI sensor set resulted in identified modes with the best cross-orthogonality with the FE target modes. However, for the triaxially-constrained example, the KE sensor set resulted in identified modes with the best cross-orthogonality with FE target modes. In both constrained and unconstrained cases the EVP technique resulted in identified modes with poor cross-orthogonalities with FE mode shapes. However, the EVP and OBS triaxially constrained sensor sets showed an improvement over the unconstrained sets. This is unusual because as a rule, the constrained sets do not perform as well as the unconstrained sets.

7.5 Effect of Model Error

In order to investigate the effect that model error has on the various placement techniques, error was added to the original Guyan-reduced FEM of the MPI structure as seen in Figure 7.11. Specifically, 1/3 of the struts' cross-sectional areas were decreased by 20%, 1/3 of the struts' cross-sectional areas were increased by 20%, and the remaining 1/3 of the struts were unchanged.

The resulting differences in pre-corrupted and post-corrupted model frequencies and mode shapes are listed in Table 7.3. The second column represents the percent differences in the frequencies of the two models. The third column represents the root mean squared (RMS) values of the absolute differences in the mode shapes of the two models. The differences between the pre- and post-corrupted model mode shapes are shown pictorially in Figure 7.12. The true modes are plotted along the horizontal axis and the corrupted modes are plotted along the vertical axis.

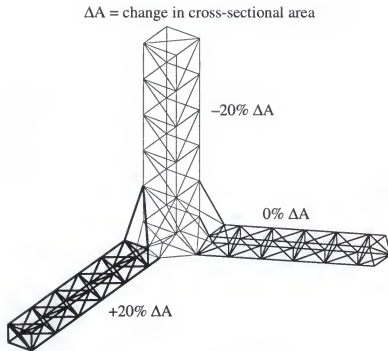


Figure 7.11 Model Error Added to MPI FEM

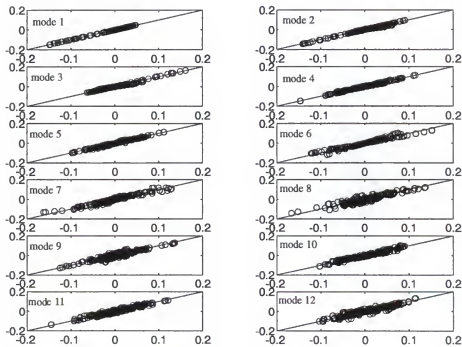


Figure 7.12 True vs. Corrupted MPI Mode Shapes

Table 7.3 Difference Between Pre- and Post-Corrupted Model Frequencies and Mode Shapes

MODE	Frequency % difference	Mode Shape RMS values
1	3.15	0.90 e-3
2	3.23	5.20 e-3
3	2.01	5.20 e-3
4	3.27	4.70 e-3
5	1.27	5.60 e-3
6	1.27	10.9 e-3
7	1.76	13.9 e-3
8	0.45	11.8 e-3
9	2.23	9.00 e-3
10	3.47	10.4 e-3
11	0.12	14.7 e-3
12	1.96	14.1 e-3

7.5.1 Excitation Placement with Model Error

Once error was introduced into the MPI FEM, the GMIF and GCON excitation placement techniques using the corrupted FEM were run. The GMIF derived excitations for the uncorrupted and corrupted models are pictured in Figure 7.13, and the GCON derived excitations for the uncorrupted and corrupted models are pictured in Figure 7.14. The GMIF excitation placement changed slightly when the model error was added; only node 77 switched to node 76 when model error was added. The GCON excitation moved the shaker from the mid span to the tip of the left boom. The directions for all of the exciters were changed when model error was added.

In order to evaluate the excitations obtained using the corrupted FEM, the time response of the MPI structure to impacts at the new excitations was numerically simulated using the original uncorrupted model. This time response was then partitioned to the uncorrupted unconstrained EI sensor set of section 7.4.1 and was sent to ERA for identification. As in the case of the uncorrupted model excitations, the target frequencies and mode shapes were

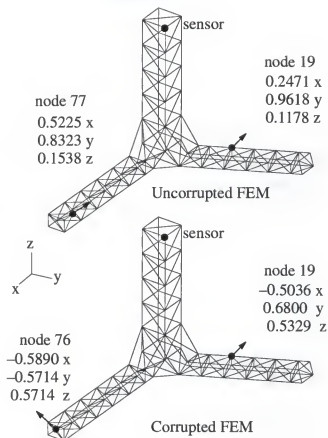


Figure 7.13 GMIF Derived Excitation Locations

successfully identified based on percent difference and cross-orthogonality calculations. Based on these results, the error added to the FEM had little to no effect on the excitation placement configurations' success in exciting the uncorrupted target mode shapes of the structure for both the GMIF and GCON excitation placement techniques.

7.5.2 Sensor Placement with Model Error

Both the unconstrained and triaxially constrained sensor placement problems were evaluated after error was added to the FEM using the six placement techniques previously discussed. The changes in sensor set configurations for the unconstrained and constrained sets are shown pictorially in Figure 7.15 and Figure 7.16. The original sensors placed using the uncorrupted FEM are represented by the boxes. Any sensors that were removed from the original sensor set after model error was introduced are represented by circles and any

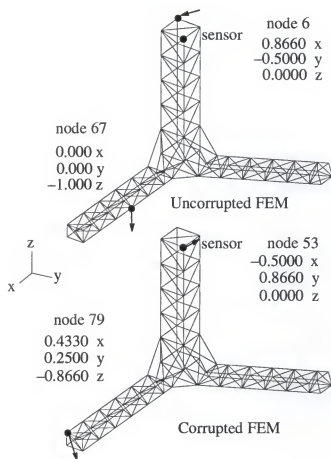


Figure 7.14 GCON Derived Excitation Locations

sensors that were added to the original set after model error was introduced are represented by triangles.

The total numbers of sensors that changed for the unconstrained and triaxially constrained sensor sets after model error was introduced are listed in Table 7.4. The general distribution of the sensors was mostly maintained after model error was added for all of the unconstrained sensor sets except for the MIF sensor set. For the constrained sensor sets, five of the six placement techniques resulted in a changed sensor set after model error was added. The EI technique moved one triax-set from the main boom tip to mid-boom. The KE technique moved one triax-set from the left extending boom tip to mid-extending-boom, and the EVP technique moved a triax-set from the left extending boom to the main boom. The AKE technique resulted in no sensor change after model error was added. The OBS and MIF

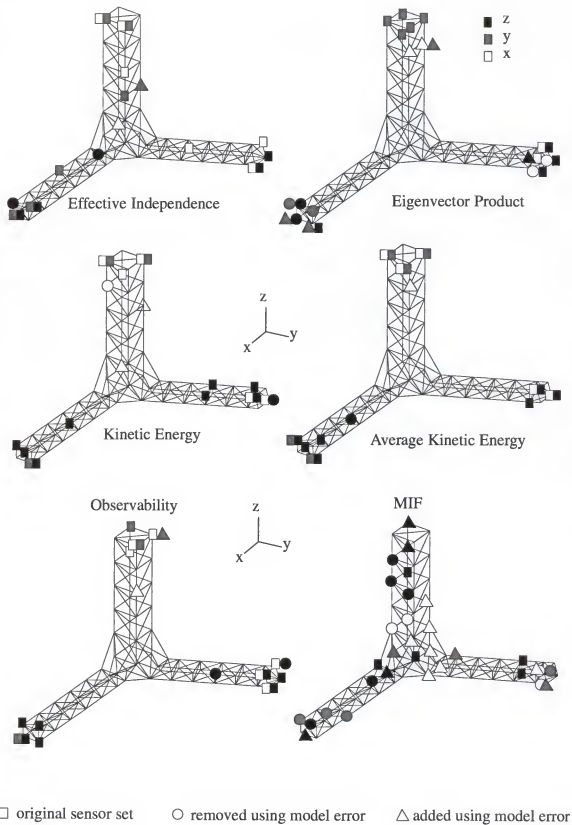


Figure 7.15 Model Error Effect on Unconstrained MPI Sensor Sets

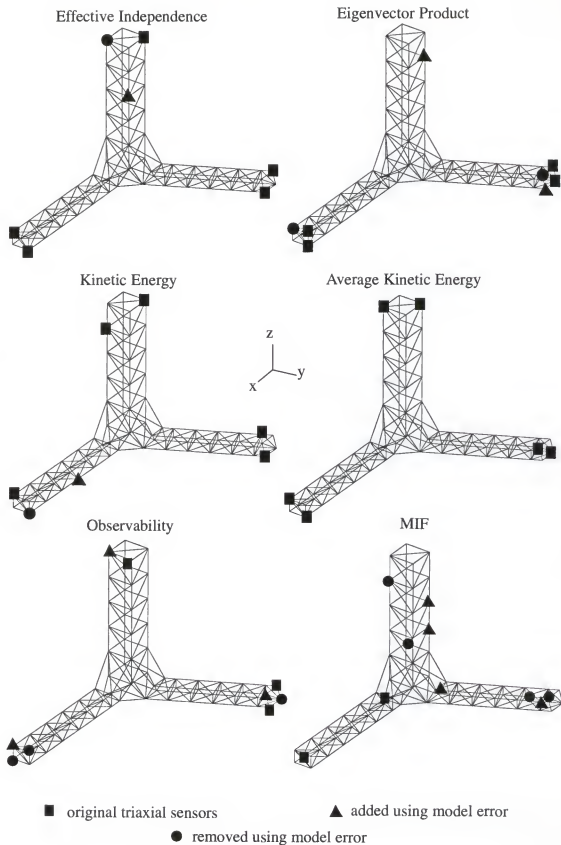


Figure 7.16 Model Error Effect on Constrained MPI Sensor Sets

technique changed over half the triaxially constrained sensors. For both the unconstrained and triaxially constrained cases, the MIF sensor placement technique was particularly sensitive to FE model error.

The original uncorrupted FEM response to the GMIF derived excitation was used to evaluate the new sensor sets obtained with the corrupted FEM. The time response discussed in the previous section was partitioned to the new sensor configurations and ERA was used to identify mode shapes and frequencies. Both the unconstrained and constrained sensor sets obtained using the corrupted FEM were successful in identifying the target frequencies within 1%, for all six techniques evaluated. The resulting cross-orthogonalities between identified (using error sensor sets) and original FEM mode shapes were calculated and are pictured in Fig. 7.17 and Fig. 7.18.

Table 7.4 Number of sensors or triax sets that change when model error is added

MPI Sensor Set	EI	KE	AKE	EVP	OBS	MIF
unconstrained	2 of 18	2 of 18	1 of 18	6 of 18	2 of 18	16 of 18
constrained	1 of 6	1 of 6	0 of 6	2 of 6	3 of 6	4 of 6

For the unconstrained sensor sets, the EI, KE, AKE, and MIF techniques resulted in generally acceptable cross-orthogonality values for the twelve target modes shown in Fig. 7.17. Only a few off-diagonal entries of the cross-orthogonalities resulting from these sensor configuration were above the acceptable limit of <0.02 for primary modes, but were still within the acceptable limit of <0.10 for secondary modes. The error added to the model in this example had little effect on the placement techniques' success in identifying sensor configurations which resulted in successful modal information identification. The EVP and OBS techniques resulted in poor cross-orthogonalities as was the case when the uncorrupted model was used.

For the triaxially constrained sensor configuration, the model error did not greatly affect the uncorrupted cross-orthogonality results for the EI, KE, AKE, and MIF techniques, as

shown in Fig. 7.18. Even though these cross-orthogonalities are not as good as those obtained with no model error, they still lie within acceptable limits previously discussed. Therefore, the error added to the model in this example had little effect on the constrained placement problem for the EI, KE, AKE, and MIF techniques. For the EVP technique, the model error resulted in a new triaxially constrained configuration which out-performed the uncorrupted configuration by chance as can be seen by the cross-orthogonalities pictured in Fig. 7.18. This is probably due to the fact that a triax-set was moved to the previously uninstrumented main boom. Even though an improvement can be seen here, several of the cross-orthogonalities are above the acceptable limits for second mode identification (>0.10). The OBS sensor set cross-orthogonalities showed deterioration after model error was added, especially for higher modes.

7.6 Computational Cost

The size of the FEM used in both the excitation and sensor placement techniques is the basic factor in the computational cost of each technique; the larger the FEM, the greater the computational cost of selecting the excitations and sensors. This computational effort is generally worthwhile, compared to the cost of planning, implementing, and performing a modal test. The approximate floating point calculations for each of the techniques explored is given in Table 7.5.

For the excitation placement using the GMIF, the most expensive part of the calculation is the MIF calculation for each possible design. As the GA searches for candidate excitation locations, the MIF for each possible location must be calculated in order to evaluate the objective function. For larger FEM some steps may be taken to reduce the computation. The controllability calculation is not nearly as costly as the MIF calculation.

Most of the sensor placement techniques are less computationally intensive. For the example used in this work, the mass matrix was (240x240) DOFs and the target mode matrix was (240x12). The 8-bay truss example used in Chapter 6 had a mass matrix of (80x80)

DOFs and a target mode matrix of (80x5). The computational costs of the EVP, KE and AKE, and EI techniques were on the order of 10^2 , 10^4 , and 10^5 MATLAB flops. Therefore, an increase in computational cost of approximately order 2 can be seen when the number of DOFs and the number of target modes are approximately tripled.

Table 7.5 Floating Point Calculations for MPI Sensor and Excitation Placement

Placement Technique	Type of Placement	Floating Point Calculations
GA/Mode Indicator Function	excitation	10^8
GA/Controllability	excitation	10^6
Effective Independence	sensor	10^7
Kinetic Energy	sensor	10^6
Average Kinetic Energy	sensor	10^6
Eigenvector Product	sensor	10^3
Observability	sensor	10^4
Mode Indicator Function	sensor	10^7

One way to reduce the computational cost of the techniques evaluated, especially effective independence and GMIF techniques, is to reduce the initial set of candidate DOFs to a target set. For the size example used in this work, this reduction is not essential, but a reduction may be needed for larger models.

7.7 Conclusions

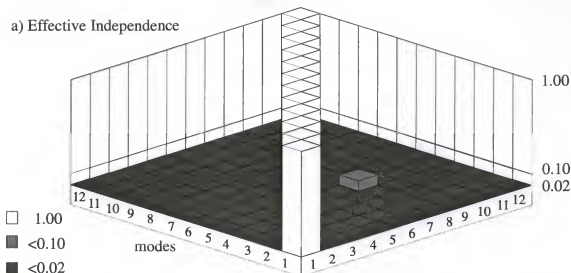
A comparative study of several pre-modal-test planning techniques was presented using the JPL/MPI testbed. Mode indicator functions calculated using a reduced FEM of the MPI structure were used in conjunction with a GA to find location and orientation of two excitation sources in order to optimally excite a chosen range of FE target modes during a modal test. The original, GMIF, and GCON excitation locations were compared using the MPI's simulated structural response to impulses applied at the exciter locations. Both the

GMIF and GCON excitation locations resulted in a time response to an impulse from which the 12 target modes were successfully identified. The original excitation locations resulted in a time response to an impulse from which there was a problem extracting modes 5 and 10. It should be noted that the original excitation was chosen by an experienced team of experimentalists/analysts, using a careful examination of the modes shapes to define a set of candidate excitations, along with MIFs to select and verify the final set. Despite this, there is still some room for improvement. This indicates the utility of a suite of pre-test planning tools to assist the designer, improving the efficiency and completeness of the process.

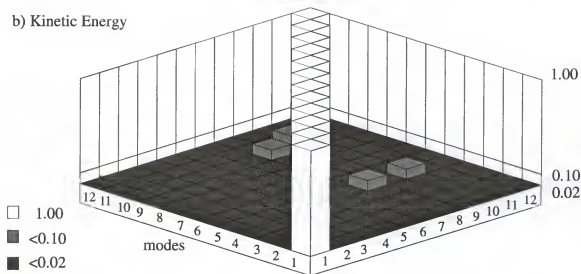
Effective independence, kinetic energy, eigenvector product techniques, observability, and mode indicator function techniques were used to place a combination of sensors on the structure for the purpose of modal identification in two ways: independent sensor placement and triaxially constrained placement. For the unconstrained and triaxially constrained sensor configurations the EI, KE, and AKE techniques were successful in identifying the target modes and frequencies from the noisy time response. The EI technique resulted in the best identification for the unconstrained set and the KE technique resulted in the best identification for the constrained set. The OBS and MIF were moderately successful in identifying target modes and frequencies from noisy data. The EVP technique was not successful in identifying the target modes for either the unconstrained or triaxially constrained sets.

Error was added to the FEM of the MPI structure in order to evaluate its effect on the placement techniques. Based on the amount of error added in this example, there was little effect seen on the excitation placement techniques, GMIF and GCON. Both techniques resulted in an excitation selection using the corrupted model that was successful in exciting the target modes. Most of the sensor placement techniques were not greatly affected by the introduction of error into the model, with the exception of the MIF sensor placement technique.

a) Effective Independence



b) Kinetic Energy



c) Average Kinetic Energy

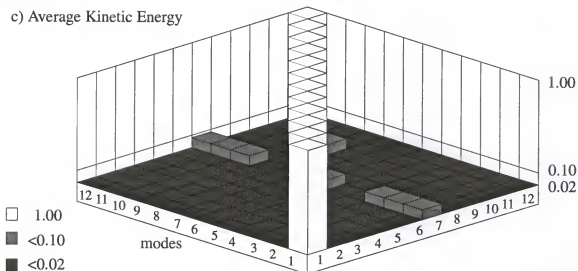
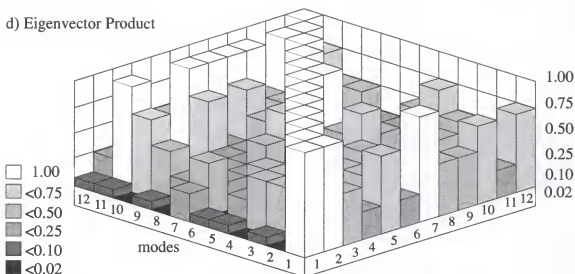
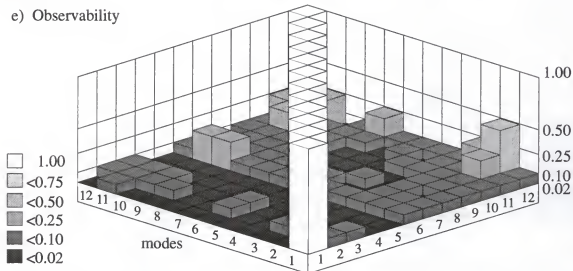


Figure 7.17 Cross-Orthogonality Between MPI Identified Modes Using Corrupted Model and Uncorrupted FEM Modes (18 Unconstrained Sensor Sets)

d) Eigenvector Product



e) Observability



f) Mode Indicator Function

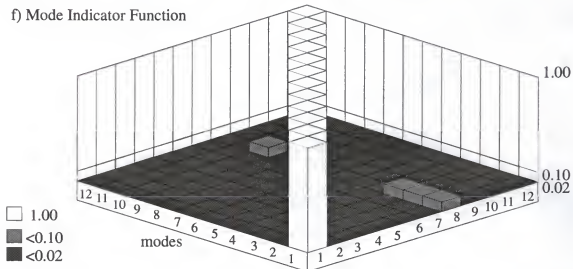
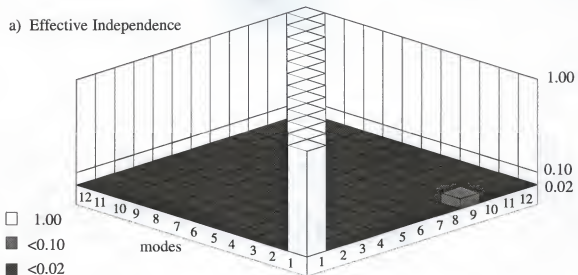
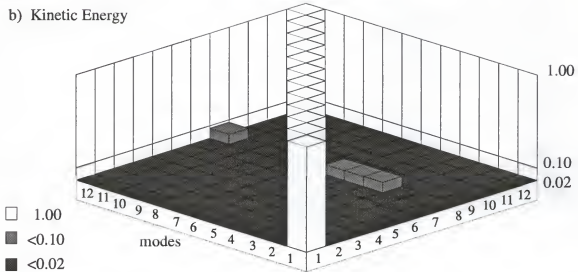


Figure 7.17 — continued

a) Effective Independence



b) Kinetic Energy



c) Average Kinetic Energy

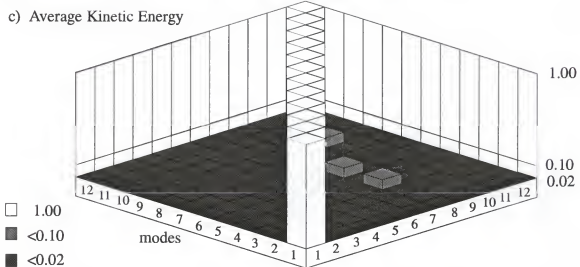
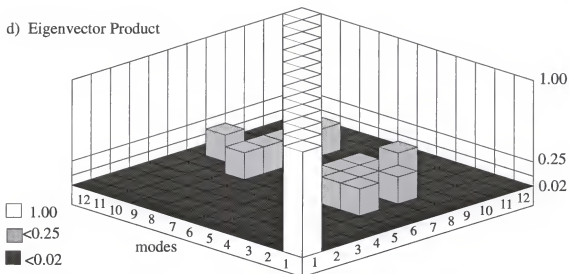
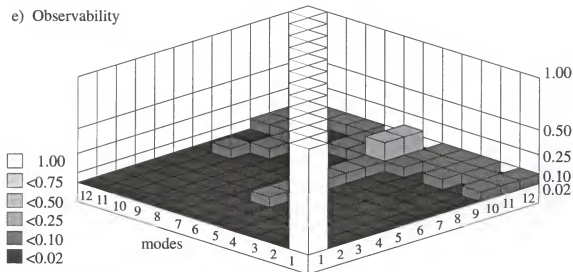


Figure 7.18 Cross-Orthogonality Between MPI Identified Modes Using Corrupted Model and Uncorrupted FEM Modes (6 Triaxially Constrained Sensors)

d) Eigenvector Product



e) Observability



f) Mode Indicator Function

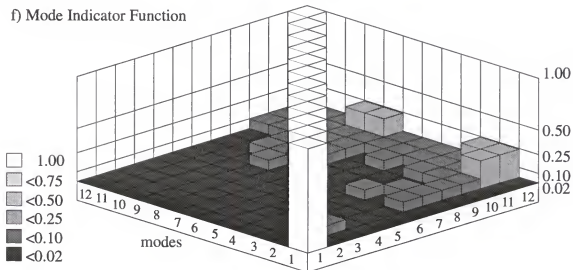


Figure 7.18 — continued

CHAPTER 8

PRE-MODAL TEST PLANNING ALGORITHM APPLICATION: CAR BODY

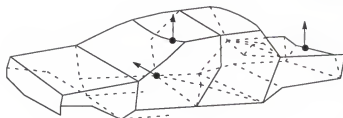
8.1 Introduction

In an effort to further examine the sensor and actuator placement strategies developed in Chapters 4 and 5 a car body FEM is considered. Recently, Carne and Dohrmann used this car FEM to explore modal test design strategies for the purpose of FE model correlation (1995). The excitation and sensor placement techniques developed in Chapter 5 are used on the same car FEM and the results are compared to those obtained by Carne and Dohrmann in their work.

8.2 Excitation Placement

Three candidate inputs were chosen by the modal test engineers based on intuition and a knowledge of the mode shapes of the car. Mode indicator functions were calculated for each of the shakers to insure their success in exciting the first 10 non-rigid body modes of the system. The GMIF and GCON algorithms were also used to place three excitation devices on the car body. The location of the shakers on the car body are shown in Figure 8.1 and are given in Table 8.1. These forces were constrained to be in any 0, 30, 45, 60, or 90 degree orientation in the x,y, and z planes. A comparison of the minimum MIF values of the 3 forces for all of the techniques is given in Table 8.2.

Original shaker location



GMIF shaker location



GCON shaker location

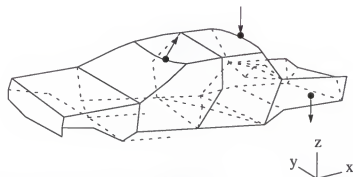


Figure 8.1 Car Body Shaker Locations

Table 8.1 Car Body Excitation Location and Orientation

Excitation	node	x-direction	y-direction	z-direction
original	100331	0	0	1.0
	100309	0	1.0	0
	100778	0	0	1.0
GMIF	100129	-0.5	0.9	0
	100226	0	0	1.0
	100780	0	0.5	0.9
GCON	100773	0.2	-0.4	0.9
	100598	0	0	-1.0
	100219	0	0	-1.0

Table 8.2 Mode Indicator Function Values for Various Excitation Placements

Mode Number	Modal Test	GMIF	GCON
1	0.01	0.01	0.00
2	0.01	0.00	0.01
3	0.03	0.07	0.03
4	0.23	0.12	0.41
5	0.10	0.12	0.12
6	0.02	0.10	0.31
7	0.19	0.09	0.11
8	0.07	0.04	0.09
9	0.32	0.14	0.12
10	0.09	0.04	0.18
min MIF	2 / 10	6 / 10	2 / 10

The GMIF excitation was the only excitation with all MIF values less than 0.15. The original excitation resulted in a maximum MIF value of 0.3 for one of the 10 target modes and the GCON excitation resulted in off diagonals of 0.4 and 0.3 for 2 of the 10 target modes. Five hundred three-shaker excitation sets were generated randomly in order to compare the three excitation placements to other excitation possibilities on the structure. Five hundred random shakers were chosen because approximately 500 population members were evaluated when the GMIF algorithm was run. A MIF for the 10 target modes for each of the three forces was taken and the minimum MIF for each mode was retained for the 500 randomly located excitation sets.

The MIF values for the randomly placed shakers as well as those being compared are pictured in Figure 8.2. In Figure 8.2 the MIF values of the 500 random excitation sources are sorted and graphed. The values of the three techniques being compared are superimposed on top of each graph. The top portion of Figure 8.2 is a graph of the minimum MIF values, the middle portion of the figure is a graph of the maximum MIF values, and the bottom portion is a graph of the sum of the MIF values for the 10 target modes (i.e., GMIF algorithm objective

function value). The key portion of Fig. 8.2 is the center portion, maximum MIF value, since it is desired that the maximum MIF of the union of all excitation forces in an excitation set be as small as possible. The maximum MIF of the GMIF excitation placement is lower than 100% of the randomly placed sensor sets. The highest maximum MIF of the three excitations is the GCON excitation placement, which is higher than approximately 60% of the randomly placed excitation sets.

The angle between the sub-spaces of the mode shapes and the subspaces of the input direction cosines was used in the GCON algorithm to find an excitation location which minimizes this angle for all of the target modes. The degree of controllability angle was calculated for the 500 randomly generated excitations as well as for original and GMIF excitation locations. Graphs of these values are pictured in Figure 8.3. The top portion of Figure 8.3 is the minimum degree of controllability angle, the middle portion is a graph of the maximum degree of controllability angle, and the bottom graph is a sum of the degree of controllability angles for the target modes (i.e., GCON algorithm objective function value). The GCON excitation placement outperformed all of the random excitations based on the controllability calculations. A comparison of the degree of controllability angles for each excitation is given in Table 8.3.

Based on the comparison of the MIF values, the three techniques used to place excitation devices performed better than a majority of randomly placed excitation set. The genetic algorithm used to drive the MIF and controllability excitation placement algorithms resulted in excitation locations which outperformed a random set of excitations based on the values of the designed objective functions. The question arises will the techniques be computationally feasible for larger FEM. Table 8.4 gives the floating point calculation required to place the excitation sets using the car body FEM. The GMIF technique resulted in a more successful excitation set based on MIF values than an exhaustive search of 500 random excitation sets, and both techniques required the same floating point calculations.

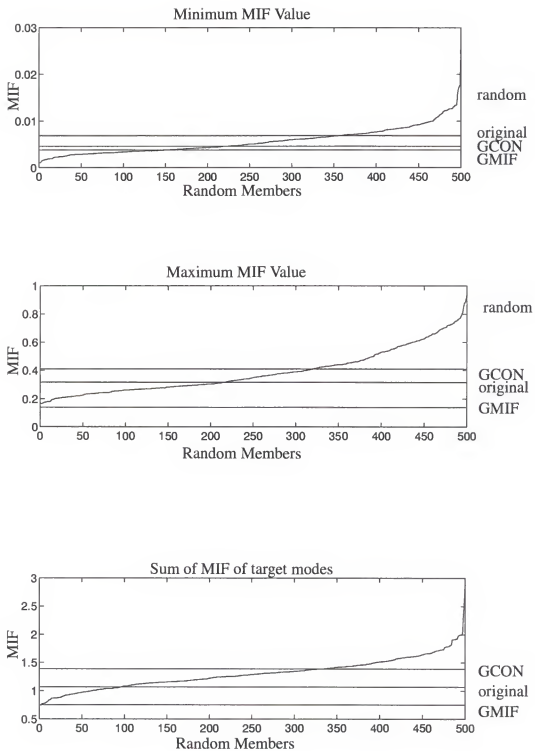


Figure 8.2 MIF Values for Excitation Placements Compared to 500 Randomly Located 3-Point Excitations

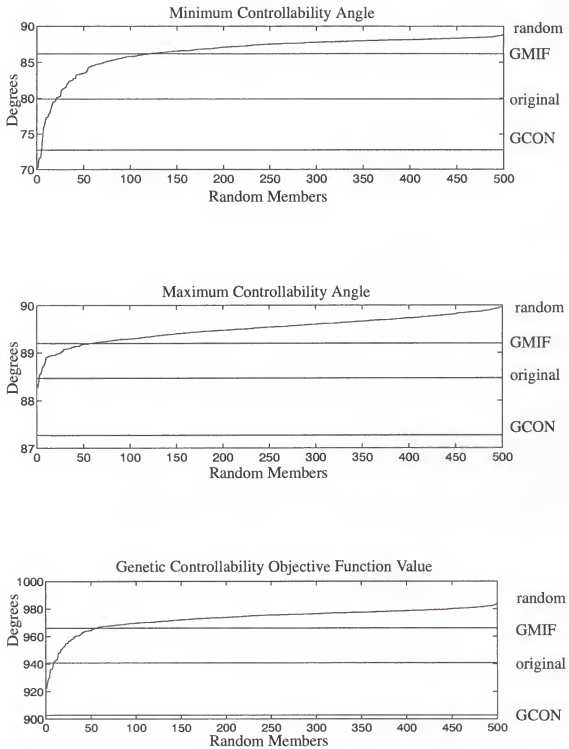


Figure 8.3 Controllability Values for Excitation Placements Compared to 500 Randomly Located 3-Point Excitations

Table 8.3 Controllability Angles (in degrees) for Excitation Placements

Mode Number	Modal Test	GMIF	GCON
1	86.3	88.7	86.6
2	88.5	87.3	86.6
3	79.9	89.2	84.3
4	88.3	88.7	82.0
5	84.3	87.6	78.3
6	88.3	88.6	78.9
7	85.8	87.2	73.4
8	84.8	87.1	72.7
9	84.9	87.2	86.3
10	83.4	86.2	87.3
min controllability angle	2 / 10	0 / 10	8 / 10

Table 8.4 Excitation Placement Techniques Floating Point Calculations

Excitation Placement Technique	Floating Point Calculations
GMIF	10^9
GCON	10^7
500 Random	10^9

In order to reduce the computational cost of the GMIF technique, a method of reducing the FEM DOFs down to a candidate set should be explored. The maximum kinetic energy or maximum average kinetic energy would be a good candidate. The full FEM mass and mode shape matrices would be used to calculate the KE energy matrix at a cost of $m(2n^2+n)$ floating point calculations (where n is the number of DOFs and m is the number of target modes). The DOFs with the maximum kinetic energy or maximum average kinetic energy over all of the target modes will be chosen as the reduced candidate DOFs for excitation

placement. The FE mode shape matrix will be partitioned to the reduced candidate DOF set and sent to the GMIF excitation placement algorithm.

8.3 Sensor Placement

Sensors are placed on the car FEM using effective independence, observability, and MIF techniques. The sensors being placed are 34 triaxially constrained sensor sets in order to compare the placements to the original intuition set placed on the car body. The three derived sensor sets and the intuition sensor set are shown in Figure 8.4.

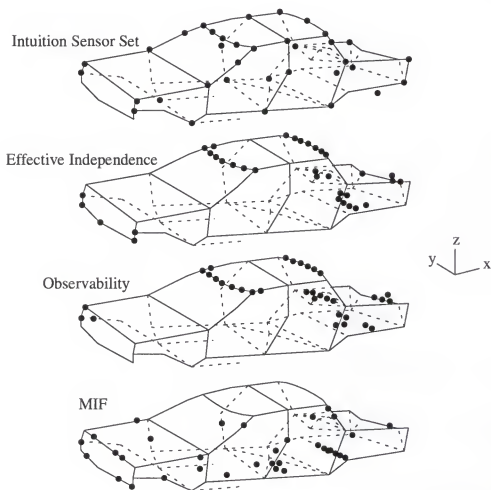


Figure 8.4 34 Triaxially Located Car Body Sensor Sets

The triaxially constrained sensor sets placed with the effective independence and observability techniques are very similar. The observability technique collocated 24 of the 34 triax sensors with the effective independence set. A majority of the sensors were placed on the roof, the package shelf, and on the front and rear ends. The intuition set distributed the sensors over the entire body. The effective independence technique is much more computationally intensive than the observability technique, which is due to the calculation of the eigensolution of the Fisher information matrix over each iteration. Table 8.5 gives a comparison of the floating point calculation required to place 34 triaxially located sensors on the car FEM. The observability technique is less computationally intensive. Based on the similarities of the EI and observability sensor configurations, the observability sensor placement technique may be used as a tool to establish a reduced set of candidate sensor DOFs or nodes for the effective independence technique to choose from. Both of the techniques tend to cluster sensors in specific locations. This is due to the fact that more sensors than target modes are being placed the structure. Once the EI and observability techniques find DOFs which indicate good target mode linear independence or observability, they tend to continue to place additional sensors in that region even though redundant information is being obtained. It is recommended that the approximate number of sensors to be placed by these techniques is equal to or slightly greater than the number of target modes to be identified. Any additional sensors required should be placed with another technique(s) such as the MIF technique.

The MIF sensor placement algorithm is the most computationally intensive of the three sensor placement techniques due to the iterative MIF calculations of the various sensor sets. However the distribution of the sensors placed using MIF calculations is more even over the entire body. This allows for better mode shape visualization, which is an important aspect of modal test data. The MIF technique did not place any sensors on the roof package of the car which contradicts the EI and observability sets. The MIF sensor configuration would

therefore be a good compliment to the EI sensor sets due to the new information it would provide about the car body.

Table 8.5 Triaxial Sensor Placement Techniques Floating Point Calculations

Sensor Placement Technique	Floating Point Calculations
MIF	10^8
Effective Independence	10^8
Observability	10^5

CHAPTER 9

CONCLUSIONS AND FUTURE WORK

This study investigated the use of genetic algorithms in the areas of finite element model refinement and pre-modal test planning excitation and sensor placement. A genetic algorithm based model refinement technique was developed. The purpose of the algorithm was to perturb FEM parameters to obtain an updated FEM with measured modal properties. The algorithm was examined using a simple FEM of a truss. The FEM of the truss was updated using numerically simulated modal data. The GMRA resulted in an updated FEM with modal properties very close to the measured modal properties. For the size of the example performed the GMRA was very effective and cost efficient. However, for very large FEMs, GMRA's true utility may lie in mapping out the design space. GMRA may be used to identify which design variables need to be changed or to locate general areas in the design space for gradient search focus.

The second scope of this study was to develop new excitation and sensor placement techniques for vibration test planning, some of which utilize genetic algorithms. An excitation technique which used the FEM to calculate a normal MIF was developed. A genetic algorithm was used to search a design space for excitation locations and orientations which exhibit sharp MIF drops for target modes. A sharp drop in MIF values at the target modes indicates that those modes are well excited. The GMIF excitation placement algorithm was evaluated on 2 FEM of increasing complexity and proved to be a powerful excitation placement tool. For the examples explored, it was both robust to noise and outperformed large random excitation selections. One drawback of GMIF is that it will be computationally intensive for large models. Some of the techniques explored such as kinetic energy may be used to reduce the full FEM down to a candidate set of node points for the

GMIF algorithm to choose from. A sensor placement algorithm was also developed using the FE MIF and was evaluated using 2 FEMs. The MIF sensor sets were the most unusual sensor configurations compared to the other placements examined in this study. Regardless of the unusual placements, the MIF sensor sets were successful in identifying the target modes required. The MIF sensor techniques distributed sensors over more of the structures than the other techniques which tended to cluster sensors in particular areas. This even distribution is well suited for mode shape visualization and possibly for damage detection purposes. However, the MIF sensor sets were particularly sensitive to FEM error. Even though the sensor sets changed after the model was corrupted, they still resulted in successful system identification for the examples examined. This result is possibly due to the overall distribution of the MIF sensor sets.

The concepts of modal controllability and observability were used to develop additional excitation and sensor placement algorithms. The degree of FE mode shape controllability was used with a genetic algorithm to search for excitation locations and orientations with high modal controllability. An excitation location with a high controllability for all of the target modes will be the best location to put energy into a system for a vibration test. The GCON algorithm was evaluated using 3 FEMs. For the examples explored, the GCON excitations outperformed a large random sample of excitations. The degree of FE mode shape observability was used to develop an optimal sensor location algorithm. DOFs with high target mode shape observability are chosen as sensor locations because the mode shapes are most observable at those points. The observability sensor placement algorithm was evaluated using 3 FEM. In general the observability technique did not locate sensor sets which were successful in identifying all of the target modes of the system. However, in the examples explored, the observability technique collocated a large number of sensor with the more computationally intensive effective independence technique. The observability technique may be used to reduce a large number of FE DOFs down to a candidate set for the EI technique to choose from.

Overall, the genetic algorithm was shown to be a feasible tool for the purpose of excitation placement. Both the GCON and GMIF algorithms resulted in excitation selections which outperformed random sets of excitations which required more calculations and intuition excitation placements. The most efficient use of these tools would be to compliment an intuition set of shakers and sensors being used in a modal test. For example, the GMIF algorithm may be used to search for an additional shakers to make up for any high target mode MIF values which are observed in an intuition set as was the case for the MPI truss. Similarly, many of the sensor placement techniques may be used together to compliment an intuition set developed by a test designer. For example m sensors may be placed using effective independence to assure linear independence of the m target modes to be measured, and the remaining sensors may be placed using the MIF technique to assure a more even distribution of the sensors. Regardless of the techniques used, all of the sensor and excitation placement algorithms are entirely dependent on the FEM of the structure that the modal test is being designed for. Therefore, the tools are only as good as the model they are based on and no more confidence than the designer has in the model should be afforded to the tools which utilize it. The true utility in these tools lies in their ability to expand on those sensor and excitation selections which are based on the intuition of the modal test designer.

Future work for this study would be an evaluation of all of excitation and sensor placement techniques using a true vibration test. All of the techniques would be used to place sensor and excitation devices on a structure. Various modal test should be performed to obtain the appropriate data for each of the techniques. The excitation placements may be evaluated on how well the target modes were excited relative to one another, and the sensor placement techniques may be evaluated on how well they extracted each of the target modes. The modal data may then be used to update the FEM of the structure. Each of the excitation and sensor placement techniques may be rerun using the updated FEM. The final evaluation would be the sensitivity of each of the techniques to the change in the FEM.

REFERENCES

- Adelman, H. M. and Haftka, R. T. (1986), "Sensitivity Analysis of Discrete Structural Systems," *AIAA Journal*, Vol. 24, No. 5, pp. 823-832.
- Andry, A. N., Shapiro, E. Y., and Chung, J. C. (1983), "Eigenstructure Assignment For Linear Systems," *IEEE Transactions on Aerospace And Electronic Systems*, Vol. AES-19, No. 5, pp. 711-729.
- Baruch, M., and Bar Itzhack, I.Y. (1978), "Optimum Weighted Orthogonalization of Measured Modes," *AIAA Journal*, Vol. 16, No. 4, pp. 346-351.
- Berman, A. and Flannelly, W. G., (1971), "Theory of Incomplete Models of Dynamic Structures," *AIAA Journal*, Vol. 9, No. 8, pp. 1481-1487.
- Berman, A. and Nagy, E. J. (1983), "Improvements of a Large Analytical Model Using Test Data," *AIAA Journal*, Vol. 21, No. 8, pp. 1168-1173.
- Carne, T. G., Mayes, R. L., and Levine-West, M. B. (1993), "A Modal Test of a Space-Truss for Structural Parameter Identification," Proceedings of the 11th International Modal Analysis Conference, Kissimmee, FL, pp. 486-494.
- Chen, J. C. and Garba, J. A. (1980), "Analytical Model Improvement Using Modal Test Results," *AIAA Journal*, Vol. 26, No. 12, pp. 1119-1126.
- Collins, J. D., Hart, G. C., Hasselman, T. K. and Kennedy, B. (1974), "Statistical Identification of Structures," *AIAA Journal*, Vol. 12, No. 2, pp. 185-190.
- Creamer, N. G., and Hendricks, S. L. (1987), "Structural Parameter Identification Using Modal Response Data," Proceedings of the 6th VPI&SU/AIAA Symposium on Dynamics and Controls for Large Structures, Blacksburg, VA, pp. 27-38.
- Ewins, D. J. (1984), *Modal Testing: Theory and Practice*, John Wiley & Sons, New York.
- Flanigan, C. C. (1991), "Correction of Finite Element Models Using Mode Shape Design Sensitivity," Proceedings of the 9th International Modal Analysis Conference, Firenze, Italy, pp. 151-159.

- Flanigan, Christopher C., and David L. Hunt (1993), "Integration of Pretest Analysis and Model Correlation Methods for Modal Surveys," Proceedings of the 11th International Modal Analysis Conference, Kissimmee, FL, February, pp 444-448.
- Fuh J., Chen S. and Berman A. (1984), "System Identification of Analytical Models of Damped Structures," Proceedings of the 25th AIAA Structures, Structural Dynamics and Materials Conference, Palm Springs, CA, pp. 112-122.
- Goodson, R. E., and Polis, M. P. (1978), "Identification of Parameters in Distributed Systems," *Distributed Parameter Systems*, edited by W. H. Ray and D.G. Lainiotis, Dekker, New York.
- Grefenstette, J. J. (ed.), (1987), Proceedings of the Second International Conference on Genetic Algorithms and Their Applications, Lawrence Erlbaum Associates, Hillsdale, NJ.
- Hamdan, A. M. A., and Nayfeh, A. H. (1989), "Measures of Modal Controllability and Observability for First- and Second-Order Linear System," *Journal of Guidance and Control*, Vol. 12, No. 3, pp. 421-427.
- Hanagud, S., Meyyappa, M. Cheng, Y. P., and Graig, J. I. (1984), "Identification of Structural Dynamics Systems with Nonproportional Damping," Proceedings of the 25th AIAA Structures, Structural Dynamics and Materials Conference, Palm Springs, CA, pp. 283-291.
- Heylen, W., and Sas, P. (1987), "Review of Model Optimization Techniques," Proceedings of the 5th International Modal Analysis Conference, Orlando, FL, pp. 1177-1182.
- Holland, J. H. (1975), *Adaptation in Natural and Artificial Systems*, The University of Michigan Press, Ann Arbor.
- Hunt, D. L., Vold, H., Peterson, E. L., and Williams, R. (1984), "Optimal Selection of Excitation Methods for Enhanced Modal Testing," Proceedings of the 25th AIAA Structures, Structural Dynamics and Materials Conference, Palm Springs, CA, pp. 1023-1030.
- Ibrahim, S.R. and Saafan, A.A., (1987), "Correlation of Analysis and Test in Modeling of Structures, Assessment and Review," Proceedings of the 5th International Modal Analysis Conference, Orlando, FL, pp. 1651-1660.
- Inman, D.J. and Minas, C. (1990), "Matching Analytical Models with Experimental Modal Data in Mechanical Systems," *Control and Dynamics Systems*, Vol. 37, pp. 327-363.
- Jarvis, B. (1991), "Enhancement to Modal Testing Using Finite Elements," *Sound and Vibration*, Vol. 8, pp. 28-30.
- Juang, J., and Pappa, R. (1985), "An Eigensystem Realization Algorithm for Modal Parameter Identification and Model Reduction," *Journal of Guidance and Control*, Vol. 8, pp. 620-627.

- Juang, J., and Rodriguez, G. (1979), "Formulations and Applications of Large Structure Actuator and Sensor Placements," Proceedings of the 2nd VPI&SU/AIAA Symposium on Dynamics and Control of Large Flexible Spacecraft, VPI, Blacksburg, VA, pp. 247-262.
- Kabe, A. M. (1985), "Stiffness Matrix Adjustment Using Mode Data," *AIAA Journal*, Vol. 23, No. 9, pp. 1431-1436.
- Kailath, T. (1980), *Linear Systems*, Prentice-Hall, Englewood Cliffs, NJ.
- Kammer, D. C. (1991), "Sensor Placement for On-Orbit Modal Identification and Correlation of Large Space Structures," *Journal of Guidance, Control, and Dynamics*, Vol. 15, No. 2, pp. 251-259.
- Kammer, D. C. (1987), "Test-Analysis Model Development Using an Exact Model Reduction," *International Journal of Analytical and Experimental Modal Analysis*, Vol. 2, No. 4, pp. 175-179.
- Kaouk, M. (1993), "Structural Damage Assessment and Finite Element Model Refinement Using Measured Modal Data," dissertation, University of Florida, Gainesville.
- Kashangaki, T. A. L. (1992), "Ground Vibration Tests of a High Fidelity Truss for Verification of on Orbit Damage Location Techniques," NASA Technical Memorandum 107626, May.
- Kientzy, D., M. Richardson, and K. Blakely (1989), "Using Finite Element Data to Set Up Modal Tests," *Sound and Vibration*, Vol. 6, pp 16-23.
- Larson, C. B., Zimmerman, D. C., and Marek, E. L. (1994), "A Comparison of Modal Test Planning Techniques: Excitation and Sensor Placement Using the NASA 8-Bay Truss," Proceedings of the 12th International Modal Analysis Conference, Honolulu, HI, pp. 205-211.
- Laub, A. J. and Arnold, W. F. (1984), "Controllability and Observability of Linear Matrix Second-Order Models," *IEEE Transactions on Automatic Control*, Vol. AC-29, No. 2, pp. 163-165.
- Le Pourhiet, A., and Le Letty, L. (1978), "Optimization of Sensor Locations in Distributed Parameter System Identification," *Identification and System Parameter Estimation*, North Holland Publishing, Amsterdam, pp. 1681-1592.
- Levine-West, M., Kissil, A., and Milman, M. (1994), "Evaluation of Mode Shape Expansion Techniques on the Micro-Precision Interferometer Truss," Proceedings of the 12th International Modal Analysis Conference, Honolulu, HA, pp. 212-218.
- Martinez, D., Red-Horse, J. and Allen, J. (1991), "System Identification Methods for Dynamic Structural Models of Electronic Packages," Proceedings of the 32nd AIAA

- Structures, Structural Dynamics and Materials Conference, Baltimore, MD, pp. 2336-2346.
- Matzen, V.C. (1987), "Time Domain Identification of Reduced Parameter Models," Proceedings of the SEM Spring Conference on Experimental Mechanics, Houston, Texas, pp. 401-408.
- O'Callahan, J.C., Avitabile P.A. and Riemer, R. (1989), "System Equivalent Reduction Expansion Process (SEREP)," Proceedings of the 7th International Modal Analysis Conference, Las Vegas, NV, pp. 29-37.
- Omatu, S., Koide, S., and Soeda, T. (1978), "Optimal Sensor Location for Linear Distributed Parameter Systems," *IEEE Transactions on Automatic Control*, Vol. AC-23, No. 4, pp. 665-673.
- Qureshi, Z. H., and Goodwin, G. C. (1980), "Optimum Experimental Design for Identification of Distributed Parameter Systems," *International Journal of Control*, Vol. 31, No. 1, pp. 21-29.
- Red-Horse, J. R., Marek, E. L., Levine-West, M. (1993), "System Identification of the JPL Micro-Precision Interferometer Truss: Test-Analysis Reconciliation," Proceedings of the 34th AIAA/ASME Structures, Structural Dynamics, and Materials Conference, LaJolla, CA, pp. 3353-3365.
- Rodden, W. P. (1967), "A Method for Deriving Structural Influence Coefficients from Ground Vibration Tests," *AIAA Journal*, Vol. 5, No. 5, pp. 991-1000.
- Salama, M., Rose, T., and Garba, J. (1987), "Optimal Placement of Excitations and Sensors for Verification of Large Dynamical Systems," Proceedings of the 28th AIAA/ASME Structures, Structural Dynamics, and Materials Conference, San Diego, CA, pp. 1024-31.
- Sawaragi, Y., Soeda, T., and Samatu, S. (1978), *Modeling, Estimation and Their Application for Distributed Parameter Systems*, Lecture Notes in Control & Information Science, Vol. 11, Springer-Verlag, Berlin, Germany.
- Schaffer, J.D. (ed.) (1989), Proceedings of the Third International Conference on Genetic Algorithms and Their Applications, Morgan Kaufmann Publishers, Inc., San Mateo, CA.
- Shah, P. C. and Udwadia, F. E. (1978), "Methodology for Optimal Sensor Locations for Identification of Dynamic Systems," *Journal of Applied Mechanics*, Vol. 45, pp. 188-196.
- Smith, S. W. and Beattie, C. A., (1990), "Simultaneous Expansion and Orthogonalization of Measured Modes for Structure Identification," Proceedings of the AIAA Dynamic Specialist Conference, Long Beach, CA, pp. 261-270.

- Udwadia, F. E., and Garba, J. A. (1985), "Optimal Sensor Locations for Structural Identification," JPL Proceedings of the Workshop on Identification and Control of Flexible Space Structures, April, pp. 247-261.
- Williams, R., Crowley, J., and Vold, H., "The Multivariant Mode Indicator Function in Modal Analysis," Proceedings of the 3rd International Modal Analysis Conference, 1985.
- Yu, T. K., and Seinfeld, J. H. (1973), "Observability and Optimal Measurement Locations In Linear Distributed Parameter Systems," *International Journal of Control*, Vol. 18, No. 4, pp. 785-799.
- Zimmerman, D. C. (1993), "A Darwinian Approach to the Actuator Placement Problem With Nonnegligible Actuator Mass," *Mechanical Systems and Signal Processing*, Vol. 7, No. 4, pp. 363-374.
- Zimmerman, D. C. and Smith S. W., (1992), "Model Refinement and Damage Location for Intelligent Structures," book chapter in *Intelligent Structural Systems*, edited by H. S. Tzou, Kluwer Academic Publishers, Boston.
- Zimmerman, D.C., and Widengren, W. (1990), "Model Correction Using a Symmetric Eigenstructure Assignment Technique," *AIAA Journal*, Vol. 28, No. 9, pp. 1670-1676.

BIOGRAPHICAL SKETCH


Cinnamon Buckels Larson received her Bachelor of Science in Engineering degree from the University of Florida department of Aerospace Engineering, Mechanics, and Engineering Science in May of 1990. She received a Master of Science degree from the same department in December of 1992.

I certify that I have read this study and that in my opinion it conforms to acceptable standards of scholarly presentation and is fully adequate, in scope and quality, as a dissertation for the degree of Doctor of Philosophy.



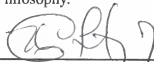
David C. Zimmerman, Chair
Associate Professor of Aerospace Engineering,
Mechanics, and Engineering Science

I certify that I have read this study and that in my opinion it conforms to acceptable standards of scholarly presentation and is fully adequate, in scope and quality, as a dissertation for the degree of Doctor of Philosophy.



Daniel Drucker
Graduate Research Professor Emeritus of
Aerospace Engineering, Mechanics, and
Engineering Science

I certify that I have read this study and that in my opinion it conforms to acceptable standards of scholarly presentation and is fully adequate, in scope and quality, as a dissertation for the degree of Doctor of Philosophy.



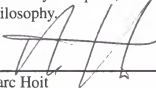
Norman Fitz-Coy
Assistant Professor of Aerospace Engineering,
Mechanics, and Engineering Science

I certify that I have read this study and that in my opinion it conforms to acceptable standards of scholarly presentation and is fully adequate, in scope and quality, as a dissertation for the degree of Doctor of Philosophy.



Peter Ifju
Assistant Professor of Aerospace Engineering,
Mechanics, and Engineering Science

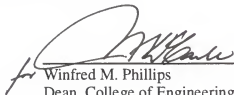
I certify that I have read this study and that in my opinion it conforms to acceptable standards of scholarly presentation and is fully adequate, in scope and quality, as a dissertation for the degree of Doctor of Philosophy.



Marc Hoit
Associate Professor of Civil Engineering

This dissertation was submitted to the Graduate Faculty of the College of Engineering and to the Graduate School and was accepted as partial fulfillment of the requirements for the degree of Doctor of Philosophy.

May 1996



Winfred M. Phillips
Dean, College of Engineering

Karen A. Holbrook
Dean, Graduate School

LD
1780
1996
. L 334

